

3-2022

A Study on the Early Stages of Degradation of Multi-component Alloy Surfaces in Extreme Environments Using the Multi-cell Monte Carlo Method

Tyler D. Dolezal

Follow this and additional works at: <https://scholar.afit.edu/etd>



Part of the [Engineering Science and Materials Commons](#)

Recommended Citation

Dolezal, Tyler D., "A Study on the Early Stages of Degradation of Multi-component Alloy Surfaces in Extreme Environments Using the Multi-cell Monte Carlo Method" (2022). *Theses and Dissertations*. 5461.
<https://scholar.afit.edu/etd/5461>

This Thesis is brought to you for free and open access by the Student Graduate Works at AFIT Scholar. It has been accepted for inclusion in Theses and Dissertations by an authorized administrator of AFIT Scholar. For more information, please contact AFIT.ENWL.Repository@us.af.mil.



**A study on the early stages of degradation of
multi-component alloy surfaces in extreme
environments using the multi-cell Monte Carlo
method**

THESIS

Tyler D. Doležal, Captain, USAF
AFIT-ENP-MS-22-M-088

**DEPARTMENT OF THE AIR FORCE
AIR UNIVERSITY**

AIR FORCE INSTITUTE OF TECHNOLOGY

Wright-Patterson Air Force Base, Ohio

DISTRIBUTION STATEMENT A
APPROVED FOR PUBLIC RELEASE; DISTRIBUTION UNLIMITED.

The views expressed in this document are those of the author and do not reflect the official policy or position of the United States Air Force, the United States Department of Defense or the United States Government. This material is declared a work of the U.S. Government and is not subject to copyright protection in the United States.

AFIT-ENP-MS-22-M-088

A STUDY ON THE EARLY STAGES OF DEGRADATION OF
MULTICOMPONENT ALLOY SURFACES IN EXTREME ENVIRONMENTS
USING THE MULTICELL MONTE CARLO METHOD

THESIS

Presented to the Faculty
Department of Engineering Physics
Graduate School of Engineering and Management
Air Force Institute of Technology
Air University
Air Education and Training Command
in Partial Fulfillment of the Requirements for the
Degree of Master of Science in Applied Physics

Tyler D. Doležal, B.S. in Physics, B.S. in Astrophysics
Captain, USAF

March 2022

DISTRIBUTION STATEMENT A
APPROVED FOR PUBLIC RELEASE; DISTRIBUTION UNLIMITED.

A STUDY ON THE EARLY STAGES OF DEGRADATION OF
MULTICOMPONENT ALLOY SURFACES IN EXTREME ENVIRONMENTS
USING THE MULTICELL MONTE CARLO METHOD

THESIS

Tyler D. Doležal, B.S. in Physics, B.S. in Astrophysics
Captain, USAF

Committee Membership:

Adib J. Samin, Ph.D.
Chair

David Weeks, Ph.D.
Member

LtCol. Whitman Dailey, Ph.D.
Member

Maj. Ryan Kemnitz, Ph.D.
Member

Abstract

Two computational tools were developed to aid in the theoretical study of solid-state system surfaces. First, A multi-cell Monte Carlo algorithm was realized based off of the existing algorithm (MC)². Then, the notoriously difficult task of generating surface slab simulation cells from a bulk structure was automated and generalized to handle simple cubic, body centered cubic, face centered cubic, and hexagonal closed packed systems. Two examples are discussed where I examined the oxidation resistance of a high-entropy alloy (HEA), Al₁₀Nb₁₅Ta₅Ti₃₀Zr₄₀, and the corrosion resistance of a ternary nickel super-alloy, Ni₇₀W₂₀Nb₁₀, against chlorine.

The investigation on the HEA system found the bulk structure to be a single body centered cubic phase in good agreement with experimental observations. The oxygen adsorbed with a strong preference towards sites with Ti and Zr and avoided sites with Nb-Al and Nb-Ta. The surface was shown to be highly reactive to oxygen, yielding a dominating oxygen coverage of 2 monolayers over a temperature range of 100 to 2600 K and oxygen pressure range from 10⁻³⁰ to 10⁵ bar. Recovering a clean surface slab was not achieved until pressure approached the vacuum condition and temperature exceeded 1900 K, demonstrating the difficulty of oxygen removal from the surface. Grand Canonical Monte Carlo simulations showed that high Nb content in the top surface layer reduced the surface reactivity to incoming oxygen. Inward oxygen diffusion at low coverage was preferred in regions rich with Zr, but slowed with the addition of Ti and Al. Diffusion rates drastically reduced at 1 monolayer, especially in the region rich with Ti and Zr, where strong metal-oxygen bonds were reported. Our results indicated that a high content of Ti and Zr increased the reactivity of the HEA surface to oxygen. The presence of Nb also enhanced resistance

to oxygen adsorption, especially when partnered with Al and Ta. Inward oxygen diffusion was likely to occur at low coverage in regions rich with Zr, but could be protected against with the addition of Al and Ti. The limitations of the present work are discussed. This study may provide insights that assist with devising short- and long-term mitigation strategies against material degradation related to high temperature oxidation.

The predicted solid-phase of the nickel super-alloy at 800 °C was a body centered tetragonal structure with an atomic concentration of Ni₇₂W₁₉Nb₉. Chlorine adsorption onto the energetically favored (110) surface showed preference to niobium which acted as a trapping sink on the top surface of the surface slab model. The findings suggested that niobium and tungsten enhanced the corrosion resistance of nickel by creating regions which were thermodynamically preferred by the incoming chlorine and less susceptible to chlorine-facilitated dissolution from the alloy. Nickel, niobium, and tungsten resisted chlorine-induced dissolution from the surface model up to a 5/15 monolayer coverage of chlorine, indicating that all constituents of this alloy possessed superior resistance to localized surface degradation such as corrosive pitting. The radiation resistance of each metallic element was considered as local chlorine content was increased. From this, it was determined that chlorine adsorption negatively impacted the radiation resistance of nickel and tungsten, and positively impacted the radiation resistance of niobium. This may point to niobium playing a dual-role in MSR applications as it could enhance both corrosion and radiation resistance of the structural alloy.

To my wife and our children.

Acknowledgements

I wish to thank Dr. Adib Samin for the education and guidance offered throughout my time at AFIT, as well as, Dr. Samin's direction and feedback which resulted in the submission of two peer-reviewed manuscripts. Lieutenant Colonel Whitman Dailey, Major Ryan Kemnitz, and Dr. David Weeks are thanked for their feedback with regards to the thesis manuscript and enhancement to the thesis defense presentation through their varying interests. Most importantly, I say thank you to my wife and children who sacrificed many weekends and evenings with me so that I could see this work through. Thank you for your love and patience.

Tyler D. Doležal

Preface

The primary deliverable of this thesis work was the implementation of a multi-cell Monte Carlo, $(MC)^2$, algorithm capable of predicting the solid phase(s) for an alloy system in its operational conditions. $(MC)^2$ delivers the capability to scanning millions of candidate alloy systems for DoD applications at low cost, i.e., approximately \$40M to execute a large-scale investigation of 5M candidate structures as compared to the $\geq \$1B$ it would cost to perform a large-scale experimental investigation. To be specific, two DoD institutions that could benefit from the $(MC)^2$ algorithm are the Air Force Research Laboratories Material and Manufacturing directorate (AFRL/RX) and the Navy Research Laboratories Center for Corrosion Sciences and Engineering. Both organizations are charged with the mission essential objectives of quantifying material corrosion and bolstering against it as it negatively impacts warfighting systems of extreme importance to national defense, i.e., Air Force aircraft systems exposed to oxidizing environments and U.S. Navy/Marine Corps vehicles deployed in seawater environments. To emphasize the usefulness of $(MC)^2$, a complete theoretical investigation was performed on an alloy that was manufactured and experimentally characterized by AFLR/RX. The $(MC)^2$ algorithm and the findings of the theoretical investigations may be useful and complementary to ongoing research endeavours within the United States Air Force and Navy and could provide insights into the design of improved structural materials for jet turbine engines.

Table of Contents

	Page
Abstract	iv
Dedication	vi
Acknowledgements	vii
Preface	viii
List of Figures	xi
List of Tables	xv
I. Computational Tools	1
1.1 Introduction	1
1.2 MC2	1
1.3 Walk-through of the Routine	3
1.3.1 Prepare VASP Input Files	3
1.3.2 Execute the algorithm	5
1.3.3 Post-processing	7
1.4 Generating MC2 Sim-cells	9
1.5 Surface Slab Generator	10
II. Theoretical Background	11
2.1 Foundations of (MC) ²	11
2.2 Density Functional Theory	14
III. Oxidation of a HEA surface	21
3.1 Introduction	21
3.2 Computational Methods	23
3.2.1 Bulk Structure	23
3.2.2 Surface Study	24
3.3 Results & Discussion	33
3.4 Conclusion	48
IV. Chlorine corrosion of a Ni-superalloy	50
4.1 Introduction	50
4.2 Computational Method	52
4.2.1 Bulk Structure	52
4.2.2 Surface Study	52
4.3 Results & Discussion	59

	Page
4.4 Conclusion	72
V. Conclusion	74
Appendix A. Least Squares	75
Bibliography	76

List of Figures

Figure	Page
1 (a) Results from the original code. (b) Results using the (MC) ² derivative developed here.	3
2 The steps in the (MC) ² derivative algorithm. Green is pre-flip logic, blue is the flipping logic, and orange is the decision logic.	6
3 (a) Cell 1 and 2 atomic concentration versus mc step. (b) top: cell 1 and 2 molar fraction at the final mc step, and bottom: cell 1 and 2 final atomic concentration.....	8
4 An example of the readout from a user terminal when executing the automated simulation cell creation tool	9
5 An example of the readout from a user terminal when executing the automated surface slab generator tool	10
6 The iterative process for Kohm-Sham DFT calculations	18
7 A sketch showing the relationship between a system's real potential/wavefunction and a psuedopotential/psuedowavefunction	20
8 The BCC bulk structure multiplied into a larger supercell for surface cuts. The (010), (011), and (111) surface planes are shown in red, blue, and green, respectively.....	25
9 The final configuration of the original (011) surface slab at 1 ML shown against the slabs that were enhanced in Al, Nb, and Ti content, labeled accordingly.	32
10 The initial slab configuration for the five diffusion events	33
11 The molar fraction value plotted against the MC step for the five simulation cells. Equilibrium begins approximately where the solid vertical line is drawn.....	34
12 (a) The projected density of states for BCC Configuration I. (b) State distribution over the s-, p-, and d-orbitals.	35

Figure	Page
13 The (011) surface slab generated from the body centered cubic bulk structure	36
14 (a) Successive adsorption energy plotted against the coverage. (b) The top-most layer of the surface slab with each adsorption event labeled in order from 1st to 15th O atom adsorbed. (c) The second surface layer with each adsorption event labeled in order from 16th to 30th O atom adsorbed.....	37
15 Adsorption energy per adsorbate versus oxygen coverage	38
16 (a) Full view of the initial (011) surface slab. (b) Full view of the surface slab at 2 ML. (c) The first surface layer at 0 ML. (d) the first surface layer at 1 ML. (e) The second surface layer at 0 ML. (f) The second surface layer at 2 ML.	39
17 The work function value over increasing coverage	40
18 (Panel 1) The charge transferred by members of surface layer 1, (Top Left), and surface layer 2, (Bottom Left), under 1 ML and 2 ML coverage. Two site maps of surface layer 1 and 2 have been included in the upper right corner of Panel 1 to help readers identify which members occupy which positions. (Panel 2) A side view, where b points into the page, of the surface slab showing how charge is transferred as a function of depth.....	42
19 The stability plot which was generated using the results of the thermodynamics study. Extreme temperatures and pressures were considered only for academic purposes. The shading has been assigned to indicate increasing coverage, where white represents the clean surface, purples represent low coverage, greens represent moderate coverage, and blues represents high coverage.	43

Figure	Page
20 Stability plots generated using the successive adsorption energy function with a GCMC simulation for the original slab, and a slab with increased Al, Nb, and Ti content, labeled respectively. The shading has been assigned to indicate increasing coverage, where white represents the clean surface, purples represent low to moderate coverage, and greens represent high to full coverage.	44
21 (a) The reaction pathway for the five diffusion sites at low coverage. (b) The reaction pathway for Site I, II, III at 1 ML coverage.	46
22 (a) Site I final position with one oxygen present on the surface. (b) Site I final position of 1 ML. An arrow is provided in (a) to indicate the direction the Zr moved in response to the O diffusion. This movement did not take place at 1 ML.	47
23 The body-centered tetragonal bulk structure multiplied into a larger supercell for surface cuts. The (010), (011), and (111) surface planes are shown in red, blue, and green, respectively.	53
24 The (110) surface slab with the eight hollow adsorption sites labeled. Because many of the chlorine atoms settled to a bridge adsorption site, one has been marked with a red X in the upper right corner. (b) The surface slab model with the cell bounds displayed.	55
25 The clean surface slab with the chlorine-attacked niobium, nickel, and tungsten atoms encircled in black. For this example, the green and red ring indicate the approximate areas that were scanned to introduce attacking atomic chlorine around tungsten. The same procedure was followed for the nickel and niobium attacks.	57
26 (a) The final atom percent of the three simulation cells which are labeled based on the final crystal structure they exhibited. (b) The Final Molar Fraction of the simulation cells. For reference, the initial molar fractions of each cell was 33.3% for each cell.	60

Figure	Page
27 (a) The projected density of states for the nickel (Ni), niobium (Nb), tungsten (W) alloy. (b) State distribution over the s-, p-, and d-orbitals.	61
28 The final configurations of the eight chlorine adsorption events.	62
29 The averaged bond lengths for nickel-, niobium-, and tungsten-chloride bonds. The average included metal-chloride bonds that formed across all three attack events.	64
30 The progression of the (a) nickel, (b) niobium, and (c) tungsten chlorine attacks up to a chlorine coverage of 5/15 ML. (d) The adsorption energies for the events depicted in (a) blue, (b) orange, and (c) green with the nearest metallic neighbors labeled. The green and red vertical lines indicate sites within the boundaries of the search rings shown in Figure 25.	66
31 Desorption energies for metal, M, atoms and metal-chloride, MCl_X , molecules, where M = (a) Ni, (b) Nb, (c) W and X = 1, 2, 3, 4, 5. Atomic chlorine, Cl, and molecular chlorine, Cl_2 , desorption energies are listed, as well. The (a) inset shows the location of the $NiCl_5$ data point.	69
32 The progression of the (a) nickel, (b) niobium, and (c) tungsten chlorine attacks up to a chlorine coverage of 5/15 ML. The vacancies are marked with a red X. (d) The vacancy formation energies for a nickel (blue), niobium (orange), and tungsten (green) as local chlorine content was increased. The nearest metallic neighbors to the adsorbed chlorine are labeled.	70
33 (a) Surface stability plot examining chlorine adsorption to the region rich with niobium. (b) Surface stability plot examining chlorine adsorption to the region rich with tungsten....	71
34 Parity plot for the successive adsorption energy function found using the method of least squares	75

List of Tables

Table	Page
1 The output file names and the data they hold	7
2 Simulation results for generating the bulk structure using $(MC)^2$	34
3 Lattice constants and angles of the three BCC equilibrium structures considered in this study	35
4 Average bond length for M-O compounds measured on the 2 ML surface slab	41
5 Results from the CI-NEB calculations	46
6 The adsorption energy values at 1/15 ML for the events displayed in Figure 28, listed in the same order. Three metals listed indicates a hollow site while two atoms represents a bridge site. A more positive value indicates a more favorable reaction.....	63
7 Coefficient values for the successive adsorption energy function found using the method of least squares	75

A STUDY ON THE EARLY STAGES OF DEGRADATION OF
MULTICOMPONENT ALLOY SURFACES IN EXTREME ENVIRONMENTS
USING THE MULTICELL MONTE CARLO METHOD

I. Computational Tools

1.1 Introduction

This chapter is dedicated to the discussion of the computational tools I developed during my time here at AFIT. Following this chapter are two examples where I used the tools to investigate the oxidation resistance and chlorine-based corrosion resistance of candidate alloy systems.

1.2 MC2

The $(MC)^2$ derivative discussed throughout this document is based on the 2019 algorithm [1] with the updated acceptance criteria derived in the 2020 paper [2]. This section will outline the procedure through a detailed example where $(MC)^2$ is used to study the Gold-Platinum (AuPt) system at $T = 800$ K, $P = 0$ Pa. Each cell has a corresponding molar fraction, which is calculated using the lever rule,

$$\mathbf{X}\mathbf{F} = \mathbf{C} \quad (1)$$

where \mathbf{X} is the atomic concentration matrix, \mathbf{F} is the molar fraction vector, and \mathbf{C} is the total concentration vector. This equation is solved for \mathbf{F} with the constraint that \mathbf{C} stay constant throughout the simulation period. x_{ij} is the number of atoms of element type i in simulation cell j divided by the total number of atoms in simulation

cell j . c_i is the total number of atoms of element type i in all simulation cells divided by the total number of atoms in all simulation cells. If “m” denotes the number of different elements present in a compound, \mathbf{X} will always be (m,m), \mathbf{F} (m,1), and \mathbf{C} (m,1). For the work discussed within this document, the energy and volume of each simulation cell is determined using Density Functional Theory (DFT). DFT calculations were implemented using Vienna Ab initio Simulation Package (VASP) [3, 4]. From an initial state, (MC)² attempts to “flip” one element type to another element type at random. There are two flips the algorithm can make: (1) local flip, (2) global flip. A local flip is where one cell is randomly selected, a random atom inside the selected cell is flipped to a different element type. A global flip is where the algorithm enumerates through all the simulation cells and randomly selects one atom and flips it. Once a flip has been made a DFT calculation is executed on the new configuration and the new energy (E) and volume (V) are recorded. After a flip, the pre- and post-flipped simulation cell(s) E, V, and atomic concentration matrix(ces) are passed through the acceptance criterion [2], Eq. 2, to see if it is an accepted move or not. The primed values in Eq. 3 are after a flip attempt while the un-primed values are before a flip attempt.

$$\rho_{\text{accept}}^{\text{flip}} = \min \{1, \exp(-\Delta G/k_B T)\} \quad (2)$$

$$\begin{aligned} \Delta G = & N \sum_k (f'^k u'^k - f^k u^k) + NP \sum_k (f'^k v'^k - f^k v^k) \\ & - N k_B T \left[\sum_k (f'^k \ln v'^k - f^k \ln v^k) \right. \\ & \left. + \sum_k f'^k \sum_j X_j'^k \ln X_j'^k - \sum_k f^k \sum_j X_j^k \ln X_j^k \right]. \end{aligned} \quad (3)$$

$\beta = 1/k_B T$, where k_B is the Boltzmann constant. N is the sum of all the particles across all simulation cells, m is the total number of simulation cells, and, therefore, phases. The energy and volume per number of atoms within the cell are u^k and v^k , respectively, and p is the pressure, which was 0 for all simulations discussed in this report. The molar fraction for each phase is f^k and X_j^k is the X_{jk} index of the matrix, \mathbf{X} . If the move is accepted, then the new “flipped” state becomes the next cycles’ initial state and the process continues. If the move is rejected, the algorithm does not update the initial state. Figure 1 shows the progression of the AuPt system throughout the $(MC)^2$ simulation from the original paper [1] (a) versus the $(MC)^2$ derivative developed here (b). Both algorithms predicted an Au- and Pt-dominate phase with molar fractions of 60/40 %.

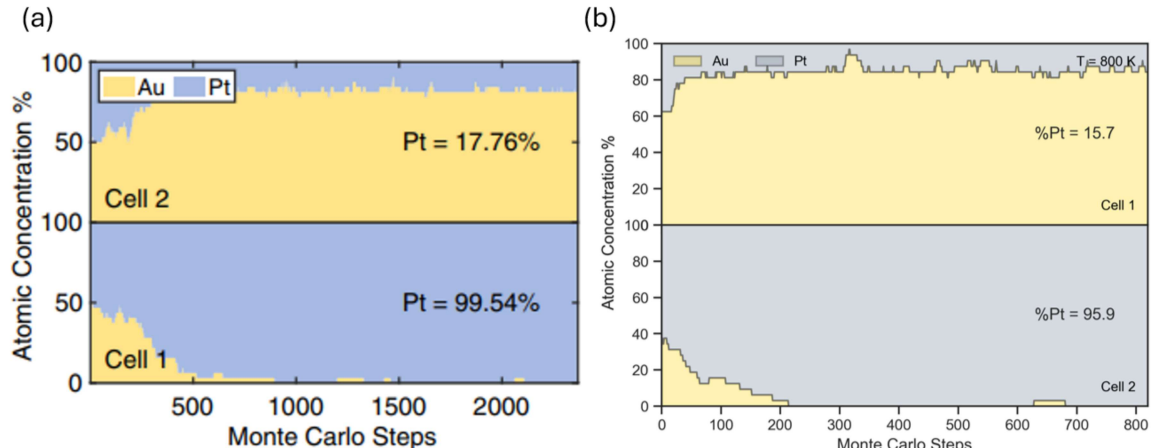


Figure 1. (a) Results from the original code. (b) Results using the $(MC)^2$ derivative developed here.

1.3 Walk-through of the Routine

1.3.1 Prepare VASP Input Files

The VASP input files are (1) INCAR, (2) POTCAR, (3) KPOINTS, (4) POSCAR. The INCAR file is where the user defines the settings for the VASP calculation. The

POTCAR file is what contains the psuedo-potential information; every element has its own psuedo-potential and own POTCAR file. For example, when examining the Au-Pt system two potential files need to be concatenated. To do this, the user must concatenate the individual element's POTCAR into one POTCAR. Usually this is handled like so,

(1) name the two POTCAR files something like Au_POTCAR and Pt_POTCAR

(2) in the command line submit the command,

(Linux/Unix) `cat Au_POTCAR Pt_POTCAR > POTCAR`

(Windows) type `Au_POTCAR Pt_POTCAR > POTCAR`

The next file is KPOINTS, which declares the number of k-points to be sampled in the Brillouin zone. Because this is reciprocal space the number of k-points should be higher for smaller simulation cells and lower for larger simulation cells. In this case, the calculations are performed with a 3x3x3 Monkhorst [5] kpoint grid. An explanation of the KPOINTS file is a grid defined as,

$$\mathbf{k} = \frac{n_1}{N_1}\mathbf{b}_1 + \frac{n_2}{N_2}\mathbf{b}_2 + \frac{n_3}{N_3}\mathbf{b}_3$$

where the user provides N_1 , N_2 , N_3 , $n_i = 0\dots, N_i - 1$, and \mathbf{b}_i are the reciprocal lattice vectors ($i = 1, 2, 3$), defined in Eq. 4, where \mathbf{a}_i are the primitive lattice vectors.

$$\mathbf{b}_1 = \frac{\mathbf{a}_2 \times \mathbf{a}_3}{\mathbf{a}_1 \cdot (\mathbf{a}_2 \times \mathbf{a}_3)} \quad , \quad \mathbf{b}_2 = \frac{\mathbf{a}_3 \times \mathbf{a}_1}{\mathbf{a}_2 \cdot (\mathbf{a}_3 \times \mathbf{a}_1)} \quad , \quad \mathbf{b}_3 = \frac{\mathbf{a}_1 \times \mathbf{a}_2}{\mathbf{a}_3 \cdot (\mathbf{a}_1 \times \mathbf{a}_2)} \quad (4)$$

Lastly, there is the POSCAR file. This file contains the geometry of the simulation cell and is usually a super-cell. Generating the POSCAR and POTCAR files has been automated to increase the accessibility of (MC)² to its users. The tool and example VASP files can be found here [6].

1.3.2 Execute the algorithm

Figure 2 is a road map of the $(MC)^2$ simulation cycle. Before calling the executable, “begin_mc2.py”, several directories and files must be prepared.

1. data/ directory
2. potcar/ directory with each species {}_POTCAR file inside
3. POSCAR1, POSCAR2
4. Concatenated POTCAR1, POTCAR2 files
5. INCAR0/1 for the initial volume/position relaxation VASP calculation
6. INCAR2 for the MC2-ISIF-3 calculations
7. INCAR-S for flipping away from singular states
8. KPOINTS
9. begin_mc2.py
10. mc2.py
11. mc2_global.py
12. myfuncs.py

For continuation runs: the logic is the same as Figure 2, except there is no initial VASP run and **C**, **X**, and **F** are read-in from the data records. The simulation picks up from the last accepted simulation state and continues making flip attempts.

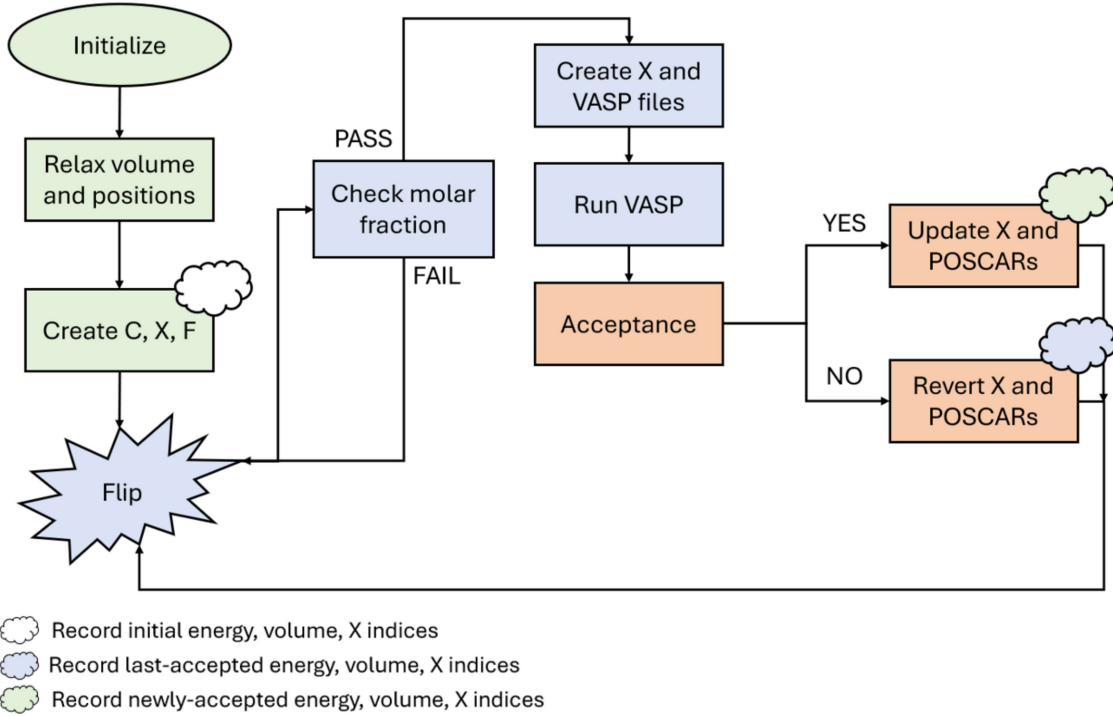


Figure 2. The steps in the $(MC)^2$ derivative algorithm. Green is pre-flip logic, blue is the flipping logic, and orange is the decision logic.

First, VASP is executed to relax each simulation cell's volume and the atomic positions. The energy and volume is recorded as the initial state. Next, the concentration vector, \mathbf{C} , and the atomic concentration matrix, \mathbf{X} , are constructed and the molar fraction vector, \mathbf{F} , is calculated. *What if \mathbf{X} is singular?* This is dealt with with the check molar fraction function. Any attempt that generates a singular matrix or molar fraction vector with elements outside the domain $[0,1]$ is not considered. A flip attempt is made, \mathbf{X} is updated with the new atomic concentrations, the trial state's POSCAR file is generated, and VASP is executed. Acceptance is determined using Eq. 2 and the Metropolis criteria [7], which can be split into 7 steps:

1. calculate $\Delta H = m \sum_{i=1}^m U'_i f'_i - m \sum_{i=1}^m U_i f_i$
2. calculate $\Delta V = \sum_{i=1}^m [f'_i \ln(V'_i) - f_i \ln(V_i)]$
3. calculate $\Delta X = \sum_{i=1}^m f'^i \sum_{j=1}^m X'^i_j \ln(X'^i_j) - \sum_{i=1}^m f^i \sum_{j=1}^m X^i_j \ln(X^i_j)$

4. plug values into expression = $\exp(-\beta\Delta H + N(\Delta V + \Delta X))$
5. choice = $\min(1, \text{expression})$
6. generate random number, $r = \text{uniform}(0,1)$
7. if $r < \text{choice}$, then accept, else, reject

1.3.3 Post-processing

The data record is saved to the /data/ directory. There are five files which are listed in Table 1.

Table 1. The output file names and the data they hold

Name	Data
energy	energy of each simulation cell
mofac	molar fraction of each phase
stepcount	the number of MC steps performed
volume	volume of each simulation cell
xdata	atomic percent data of each cell

Post-processing has been automated to increase (MC)² accessibility to the users. The post-processing tool can be found here [8]. Figure 3 includes an example of two outputs: (a) the progression of each cell's atomic concentration vs. MC step and (b) top: the final molar fraction of each cell, bottom: the final atomic concentration of each simulation cell.

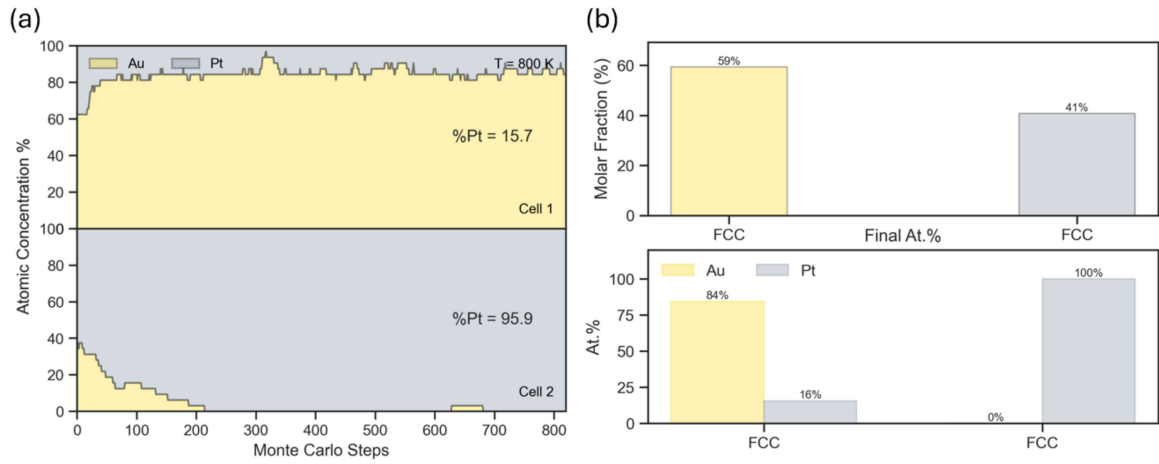


Figure 3. (a) Cell 1 and 2 atomic concentration versus mc step. (b) top: cell 1 and 2 molar fraction at the final mc step, and bottom: cell 1 and 2 final atomic concentration.

1.4 Generating MC2 Sim-cells

As mentioned previously, creating the simulation cell POSCAR and concatenated POTCAR files has been automated and is here [6]. Figure 4 is an example of using the tool.

```
----- User Inputs -----
1. Op. System (windows, linux, unix)? windows
2. Species Names (Au Pt Zr Ti etc)? Al Nb Ta Ti Zr
3. Total system concentration? 0.1 0.15 0.05 0.30 0.40
5. How many atoms total per sim cell (32 or 48)? 32
6. Generate POTCARs (y or n)? n
----- procedure initialized -----
---- Generated POSCAR1
---- Generated POSCAR2
---- Generated POSCAR3
---- Generated POSCAR4
---- Generated POSCAR5
----- procedure complete -----
```

Figure 4. An example of the readout from a user terminal when executing the automated simulation cell creation tool

1.5 Surface Slab Generator

This work taught me how to cut surface slabs from bulk super-cell structures. I developed a tool which automates the process and it can be found here [9]. An example of executing the tool is provided in Figure 5

```
|----- Welcome -----|
| Here is a list of supported surfaces, crystal lattices, and |
| atom/unit cell |
|-----|
| Lat. | 1 0 0 | 0 1 0 | 0 0 1 | 1 1 0 | 1 0 1 | 0 1 1 | 1 1 1 |
|-----|
| sc | 1 | 1 | 1 | 2 | 2 | 2 | 6 |
| bcc | 2 | 2 | 2 | 4 | 4 | 4 | 12 |
| fcc | 4 | 4 | 4 | 8 | 8 | 8 | 24 |
| hcp | 4 | 4 | 4 | 8 | 8 | 8 | 24 |
|-----|
|----- inputs -----|
*if bulk is not supercell provide: 1 1 1
1. choose a face: 110
2. lattice geometry of bulk: bcc
3. if bulk structure is a supercell
   provide the supercell dimensions* (x y z): 4 4 4
4. surface slab dimensions (x y z): 3 3 2
5. How many terminations of the bcc 110 slab? 3
6. vacuum thickness: 20
----- procedure initiating -----
1. bulk dimensions applied
2. slab supercell generated
3. vacuum layer of 20 Å added
4. updating atomic data
5. 3 termination(s) of the bcc 110 surface slab of dims (3, 3, 2)
   completed
----- procedure complete -----
----- please see POSCAR1 -----
----- please see POSCAR2 -----
----- please see POSCAR3 -----
```

Figure 5. An example of the readout from a user terminal when executing the automated surface slab generator tool

II. Theoretical Background

2.1 Foundations of $(MC)^2$

The multi-cell Monte Carlo algorithm discussed in Chapter I is a new way to predict the phase coexistence of a solid structure. The formulation of $(MC)^2$ is heavily based on the phase coexistence Gibbs ensemble Monte Carlo algorithm introduced by Panagiotopoulos [10, 11, 12]. This method introduced separate cells which represent different phases. Because equilibrium phase diagrams of mixed systems are typically reported at constant temperature and pressure, the simulation is executed under the isobaric-isothermal condition (N,P,T) . The volume of each phase, or cell, is free to change until the target pressure is reached. The derivation begins with the partition function for the isobaric-isothermal Gibbs ensemble for a mixed system represented in two cells [13]. Eq. 5 yields the number of ways to of arranging $N = n_1 + n_2$ particles between the cells α and β while holding P and T constant.

$$\begin{aligned}
Q_{NPT}^{\text{Gibbs}} &= \frac{1}{n_1! \Lambda^{3n_1} V_o} \frac{1}{n_2! \Lambda^{3n_2} V_o} \sum_{n_1^\alpha=0}^{n_1} \frac{n_1!}{n_1^\alpha! n_1^\beta!} \sum_{n_2^\alpha=0}^{n_2} \frac{n_2!}{n_2^\alpha! n_2^\beta!} \int_0^\infty dV^\alpha \exp\left(-\frac{PV^\alpha}{k_B T}\right) \\
&\times \int_0^\infty dV^\beta \exp\left(-\frac{PV^\beta}{k_B T}\right) \int d(r_1^\alpha)^{n_1^\alpha} \int d(r_2^\alpha)^{n_2^\alpha} \int d(r_1^\beta)^{n_1^\beta} d(r_2^\beta)^{n_2^\beta} \\
&\times \exp\left(-\frac{U^\alpha(n^\alpha)}{k_B T}\right) \exp\left(-\frac{U^\beta(n^\beta)}{k_B T}\right)
\end{aligned} \tag{5}$$

In Eq. 5, Λ is the thermal de Broglie wavelength, V_o is a unit of volume which makes the partition function dimensionless [14], k_B is the Boltzmann constant, r_i^k is the positions of particles of species i in cell k , and $U^k(n^k)$ is the energy of cell k . The volume dependence can be made explicit through a changing to scaled coordinates,

$s_i^k = r_i^k/(V^k)^{1/3}$, which yields,

$$Q_{\text{NPT}}^{\text{Gibbs}} = \frac{1}{n_1! \Lambda^{3n_1} V_o} \frac{1}{n_2! \Lambda^{3n_2} V_o} \sum_{n_1^\alpha=0}^{n_1} \frac{n_1!}{n_1^\alpha! n_1^\beta!} \sum_{n_2^\alpha=0}^{n_2} \frac{n_2!}{n_2^\alpha! n_2^\beta!} \int_0^\infty dV^\alpha \exp\left(-\frac{PV^\alpha}{k_B T}\right) (V^\alpha)^{n^\alpha} \\ \times \int_0^\infty dV^\beta \exp\left(-\frac{PV^\beta}{k_B T}\right) (V^\beta)^{n^\beta} \int d(s_1^\alpha)^{n_1^\alpha} \int d(s_2^\alpha)^{n_2^\alpha} \int d(s_1^\beta)^{n_1^\beta} d(s_2^\beta)^{n_2^\beta} \\ \times \exp\left(-\frac{U^\alpha(n^\alpha)}{k_B T}\right) \exp\left(-\frac{U^\beta(n^\beta)}{k_B T}\right). \quad (6)$$

From Eq. 6, the probability density function can be extracted (see [13, 15] for a detailed derivation),

$$\rho_{\text{NPT}}^{\text{Gibbs}} = \exp \left[\ln \left(\frac{n_1!}{n_1^\alpha! n_1^\beta!} \right) + \ln \left(\frac{n_2!}{n_2^\alpha! n_2^\beta!} \right) + n^\alpha \ln V^\alpha + n^\beta \ln V^\beta \right. \\ \left. - \frac{PV^\alpha}{k_B T} - \frac{PV^\beta}{k_B T} - \frac{U^\alpha}{k_B T} - \frac{U^\beta}{k_B T} \right]. \quad (7)$$

The probability of acceptance is given by the Metropolis criteria $\min\{1, \frac{\rho'}{\rho}\}$ [7], where ρ and ρ' are the probability densities of the initial and final state, respectively.

To generate the acceptance criteria for the $(\text{MC})^2$ algorithm, a series of variable changes are made in favor of the $(\text{MC})^2$ variables. If we consider two cells to represent an α and β phase with a total of $N = n^\alpha + n^\beta$ particles, we have

1. $C_m^0 = (n_m^\alpha + n_m^\beta)/N$; initial concentration of the m th species
2. $n^\alpha = f^\alpha N$; total number of particles in cell α
3. $n_1^\alpha = N f_\alpha X_1^\alpha$; number of species 1 particles in cell α
4. $X_1^\alpha = n_1^\alpha/n^\alpha$; atomic concentration of species 1 in cell α
5. $U^\alpha = N f^\alpha u^\alpha$; energy of cell α
6. $V^\alpha = N f^\alpha v^\alpha$: volume of cell α

where $u^\alpha = U^\alpha/n^\alpha$ and $v^\alpha = V^\alpha/n^\alpha$. Eq. 7 can be re-expressed in terms of the

$(MC)^2$ variables,

$$\begin{aligned} \rho_{\text{NPT}}^{\text{Gibbs}} = & \exp \left[\ln \left(\frac{(NC_1^0)!}{(Nf^\alpha X_1^\alpha)!(Nf^\beta X_1^\beta)!} \right) + \ln \left(\frac{(NC_2^0)!}{(Nf^\alpha X_2^\alpha)!(Nf^\beta X_2^\beta)!} \right) \right. \\ & + f^\alpha N \ln(Nf^\alpha v^\alpha) + f^\beta N \ln(Nf^\beta v^\beta) \\ & \left. - N(P[f^\alpha v^\alpha + f^\beta v^\beta] + f^\alpha u^\alpha + f^\beta u^\beta) / k_B T \right] \end{aligned} \quad (8)$$

which can be reduced by using the Stirling approximation on the first two terms. The final expression, with the omission of constant terms that vanish in the acceptance criteria, is given in Eq. 9.

$$\begin{aligned} \rho(f^\alpha, N, P, T) \sim & \exp(-N(P[f^\alpha v^\alpha + f^\beta v^\beta] + f^\alpha u^\alpha + f^\beta u^\beta) / k_B T) \\ & \times \exp(-Nf^\alpha[X_1^\alpha \ln X_1^\alpha + X_2^\alpha \ln X_2^\alpha - \ln v^\alpha]) \\ & \times \exp(-Nf^\beta[X_1^\beta \ln X_1^\beta + X_2^\beta \ln X_2^\beta - \ln v^\beta]) \end{aligned} \quad (9)$$

Using the Metropolis criteria, the acceptance probability for a flip move, where the initial concentrations, C_m^0 , are kept constant, which generates a new state with energy u'^α , volume, v'^α , and a molar fraction value, f'^α is,

$$\rho_{\text{accept}}^{\text{flip}} = \min \{1, \exp(-\Delta G/k_B T)\} \quad (10)$$

$$\begin{aligned} \Delta G = & N \sum_k (f'^k u'^k - f^k u^k) + NP \sum_k (f'^k v'^k - f^k v^k) \\ & - Nk_B T \left[\sum_k (f'^k \ln v'^k - f^k \ln v^k) \right] \end{aligned}$$

$$+ \sum_k f'^k \sum_j X_j'^k \ln X_j'^k - \sum_k f^k \sum_j X_j^k \ln X_j^k \Big]. \quad (11)$$

In Eq. 11, primed coordinates represent the post-flip state and unprimed represent the pre-flip state.

As flip attempts are made it is important that mass conservation is not violated and that the initial concentration of the entire system remains constant. This is enforced by use of the lever rule, which can be written as a system of equations. Eq. 12 is the lever rule expression of a binary phase problem.

$$\begin{bmatrix} C_1^0 \\ C_2^0 \end{bmatrix} = \begin{bmatrix} X_1^\alpha & X_1^\beta \\ X_2^\alpha & X_2^\beta \end{bmatrix} \begin{bmatrix} f^\alpha \\ f^\beta \end{bmatrix} \quad (12)$$

By enforcing the lever rule over all phases, the atomic fractions, X_j^k , are free to change independently such that they do not violate the conservation of mass across the entire system. As the atomic concentrations fluctuate Eq. 12 is solved to yield the updated molar fraction value for each phase. This way, the phases' growth can be tracked without needing to physically perform a mass transfer (i.e., an insert-delete move comparable to the Gibbs ensemble MC). *Special note*, the implementation discussed in Chapter I was based on the original $(MC)^2$ algorithm, therefore translational perturbations, interswap, and intraswap moves are not implemented.

2.2 Density Functional Theory

Within this work, the solid-phase prediction algorithm, $(MC)^2$, as well as, the research covered in the proceeding chapters, depended on the Vienna Ab-initio Software Package¹ (VASP) [16]. This computational toolkit employs Density Functional Theory (DFT), a computational method which is rooted in quantum mechanical

¹In general, $(MC)^2$ can be executed using MC or molecular dynamics simulations if the system is described by a potential.

modelling. This section will provide the theoretical derivation of DFT.

DFT models a system of atoms, ions with electrons, through the application of the Born-Oppenheimer approximation [17], where it is assumed that the wave functions of the atomic nuclei and electrons can be treated separately based on the fact that the nuclei are much heavier than the electrons. Under this approximation, the nuclei generate an external, potential V . The electronic system is described by a stationary state wavefunction, Ψ , which satisfies the time-independent many-body Schrödinger equation,

$$\left[\sum_{i=1}^N \left(-\frac{\hbar^2}{2m_i} \nabla_i^2 \right) + \sum_{i=1}^N V(\vec{r}_i) + \sum_{i < j}^N U(\vec{r}_i, \vec{r}_j) \right] \Psi = E\Psi \quad (13)$$

Now, at this point, one possible method to solving this equation is to expand the wavefunction into a Slater determinant which can then be solved via the Hartree-Fock method. The downside to this approach is it is extremely computationally expensive, especially if examining a large system of atoms. This is precisely where DFT generates its usefulness. In 1964, Hohenberg and Kohn provided two theorems [18],

Theorem I: *For any system of interacting particles in an external potential $V(r)$, the density is uniquely determined.*

Theorem II: *A universal functional for the energy $E[n]$ can be defined in terms of the density. The exact ground state is the global minimum value of this functional.*

Proof of Theorem I

Consider two external potentials, $\hat{V}_1(\vec{r})$ and $\hat{V}_2(\vec{r})$, that differ only by a constant and give rise to the same ground state density, $\rho_0(\vec{r})$. Each system is described by a separate Hamiltonian, $\hat{H}_1(\vec{r})$ and $\hat{H}_2(\vec{r})$, which each have their own wavefunctions, $\Psi_1(\vec{r})$ and $\Psi_2(\vec{r})$. According to the variational principle, the energy [for system 1] we

obtain when using Ψ_1 will be less than the energy predicted when using Ψ_2 ,

$$E^{(1)} = \langle \Psi_1 | \hat{H}_1 | \Psi_1 \rangle < \langle \Psi_2 | \hat{H}_1 | \Psi_2 \rangle .$$

The same is true for system 2,

$$E^{(2)} = \langle \Psi_2 | \hat{H}_2 | \Psi_2 \rangle < \langle \Psi_1 | \hat{H}_2 | \Psi_1 \rangle$$

Now add the energies,

$$E^{(1)} + E^{(2)} < \langle \Psi_2 | \hat{H}_1 | \Psi_2 \rangle + \langle \Psi_1 | \hat{H}_2 | \Psi_1 \rangle \quad (14)$$

where,

$$\hat{H}_1 = \hat{T} + \hat{V}_1 \quad \text{and} \quad \hat{H}_2 = \hat{T} + \hat{V}_2$$

$$\therefore \hat{T} = \hat{H}_1 - \hat{V}_1 \quad \text{or} \quad \hat{T} = \hat{H}_2 - \hat{V}_2$$

Using the above relationships, we can write out the two expectation values on the right-hand side of Eq. 14, keeping in mind each system generates the same ground state density,

$$\langle \Psi_2 | \hat{H}_1 | \Psi_2 \rangle = \langle \Psi_2 | \hat{H}_2 | \Psi_2 \rangle + \int d\vec{r} (\hat{V}_1 - \hat{V}_2) \rho_0(\vec{r})$$

$$\langle \Psi_1 | \hat{H}_2 | \Psi_1 \rangle = \langle \Psi_1 | \hat{H}_1 | \Psi_1 \rangle + \int d\vec{r} (\hat{V}_2 - \hat{V}_1) \rho_0(\vec{r})$$

which yields,

$$E^{(1)} + E^{(2)} < E^{(1)} + E^{(2)}$$

and this is a contradiction.

Proof of Theorem II

From the first theorem, since the external potential is unique to the electronic density and since the potential, in turn, generates a unique ground state wavefunction, all observables of the system are uniquely determined. The ground state energy is determined by a unique ground state density,

$$E_0[\rho_0] = \langle \Psi[\rho_0] | \hat{H} | \Psi[\rho_0] \rangle .$$

By the variational principle, any other density will deliver an energy higher than E_0

$$E_0[\rho_0] < \langle \Psi[\rho] | \hat{H} | \Psi[\rho] \rangle$$

Therefore, one needs to minimize the total energy of the system with respect to the electron density to find the ground state energy. Whichever density minimizes the energy of the system is the ground state electron density.

Armed with the Hohenberg-Kohn theorems, the many-body electronic problem is reshaped in terms of the electron density, Eq. 15, which eliminates the electron-electron interactions, $U(\vec{r}_i, \vec{r}_j)$, term.

$$\rho(\vec{r}) = \sum_{i=1}^N |\Psi(\vec{r})|^2 \tag{15}$$

To continue, the system is described using the Kohn-Sham equation, Eq. 16, which describes a *fictitious* system of non-interacting particles that generate the same electron density as any given system of interacting particles [19].

$$\left(-\frac{\hbar^2}{2m} \nabla^2 + v_{\text{eff}}(\vec{r}) \right) \varphi_i(\vec{r}) = \epsilon_i \varphi_i(\vec{r}) \tag{16}$$

$$\rho(\vec{r}) = \sum_{i=1}^N |\varphi_i(\vec{r})|^2 \quad (17)$$

The effective potential term, $v_{\text{eff}}(\vec{r})$ is expressed as,

$$v_{\text{eff}}(\vec{r}) = V(\vec{r}) + e^2 \int \frac{\rho(\vec{r}')}{|\vec{r} - \vec{r}'|} d^3 r' + V_{\text{XC}}[\rho(\vec{r})] \quad (18)$$

where $V_{\text{XC}}[\rho(\vec{r})]$ is the functional derivative of the exchange-correlation energy, i.e.,

$$V_{\text{XC}}[\rho(\vec{r})] = \frac{\delta E_{\text{XC}}[\rho(\vec{r})]}{\delta \rho(\vec{r})} . \quad (19)$$

The Kohn-Sham equations are solved self-consistently, see Figure 6.

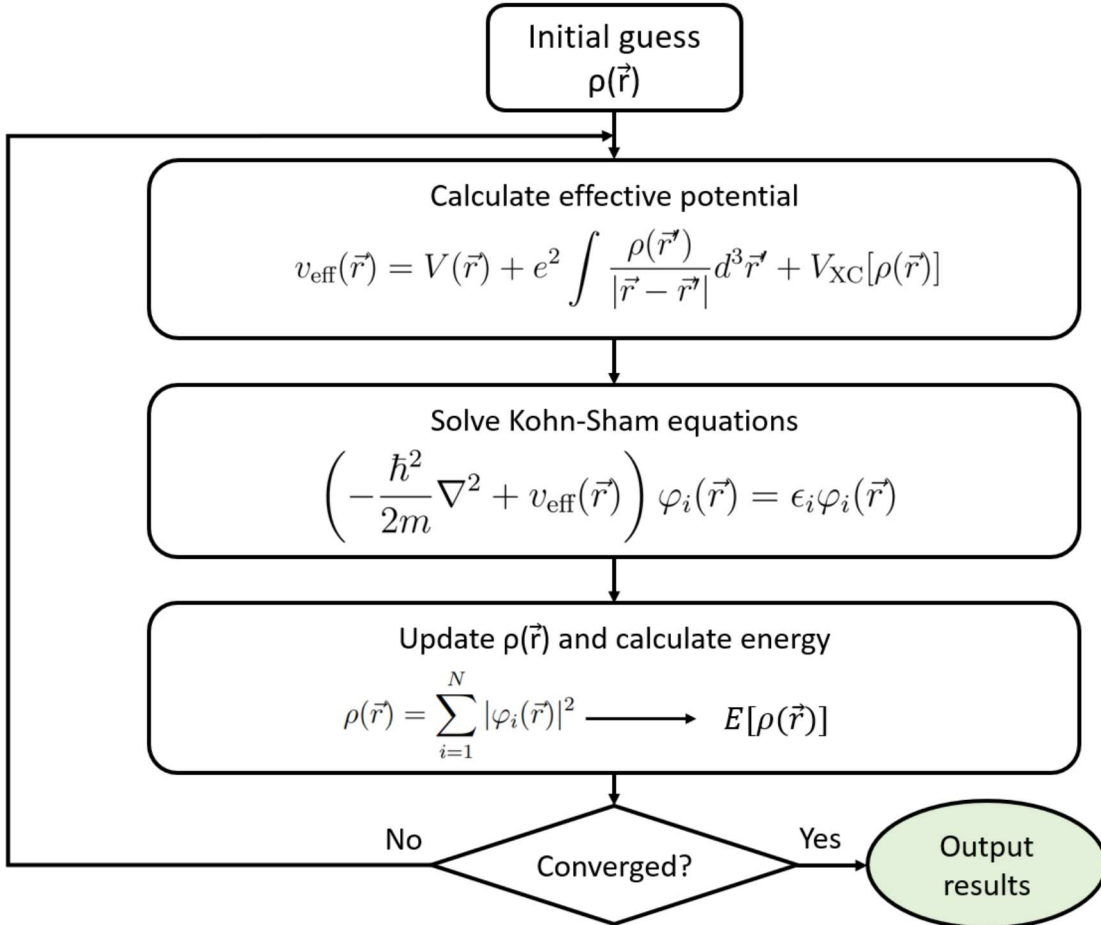


Figure 6. The iterative process for Kohn-Sham DFT calculations

Before closing, it is worth sharing a few details about the exchange-correlation functionals and the use of pseudopotentials. The exchange-correlation functionals are modeled on the uniform-electron-gas where the correlation energy is calculated using Monte Carlo methods for a large range of densities which is then parameterized to generate an exchange correlation functional. Some approximations used when calculating the functionals include the local-density approximation (LDA) and the generalized gradient approximation (GGA). The LDA limits the exchange-correlation to depend only on the electronic density value at each point in space, as opposed to any derivatives of the density or the Kohn-Sham orbitals. Because the LDA assumes the electronic density is the same everywhere it tends to underestimate the exchange energy and overestimate the correlation energy [20]. To correct for this, terms related to the gradient of the electronic density are added to account for any non-homogenous contributions. The expansion to include gradient terms is the GGA [21].

The motivation behind a pseudopotential is to reduce the computational cost of executing DFT calculations. Describing a system with a pseudopotential makes the use of the plane-wave basis set practical², as it can be used with a significantly lower cut-off energy which reduces the size to which the wavefunction basis set is expanded to, and this in turn allows for proper numerical convergence within a reasonable amount of computational resources. The pseudopotential and its corresponding pseudowavefunction are constructed such that they mirror the system they represent beyond a cut-off radius, r_c , as shown in the diagram displayed in Figure 7 [22]. In the pseudopotential system the core electrons are *frozen* and treated together with the nuclei as rigid non-polarizable ion cores. Two commonly used pseudopotentials are the norm-conserving pseudopotential and ultrasoft pseudopotentials. Norm-conserving

²The plane-wave basis set is used in VASP

psuedopotentials enforce that the norm of the psuedowavefunction be equivalent to the norm of the true wavefunction *inside* the cut-off radius. The ultrasoft approach has a softer norm-constraint and is related to the incredibly popular projector augmented wave method [4] which further increased the computational efficiency of DFT calculations.

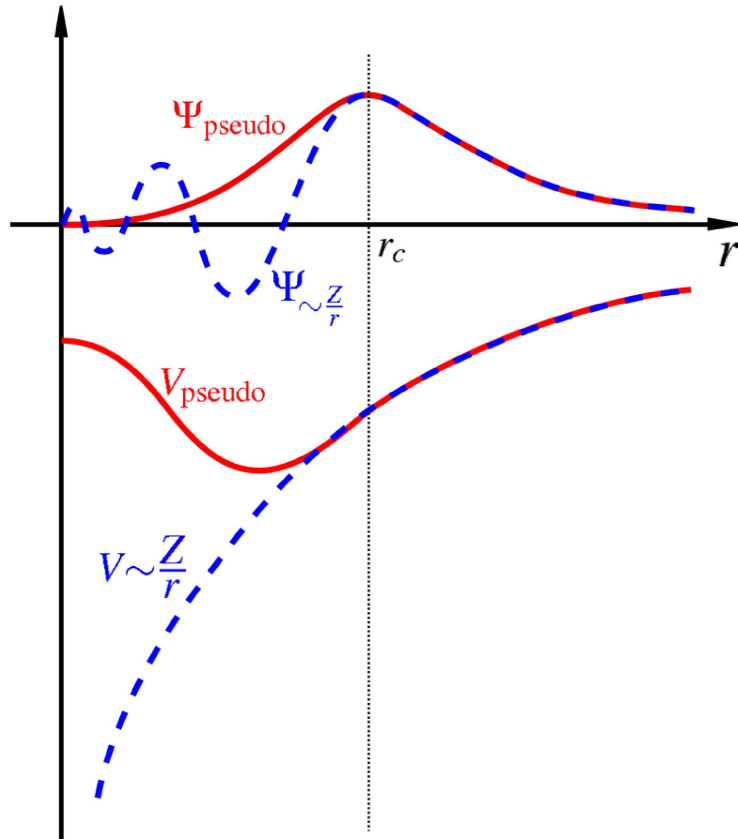


Figure 7. A sketch showing the relationship between a system's real potential/wavefunction and a psuedopotential/psuedowavefunction

III. Oxidation of a HEA surface

3.1 Introduction

High entropy alloys (HEAs) have been an area of intense research since their first mention in 2004, where Cantor et al., [23] synthesized a five component FeCrMnNiCo alloy by melt spinning and Yeh et. al, [24] produced, and coined the term HEA, several HEAs by arc melting which included Cu, Ti, Cr, Ni, Co, V, Fe, and Al. They proposed that a multi-component alloy at near equiatomic concentrations would increase the entropy of mixing to overcome the enthalpies of compound formation, resulting in a lower probability of formation of potentially deleterious intermetallics. This statement is summarized mathematically by examining the ideal entropy of mixing,

$$\Delta S_{\text{mix}} = -R \sum_{i=1}^n x_i \ln(x_i) \quad (20)$$

where R is the ideal gas constant and x_i is the atomic concentration of the i-th element. If n is to equal 5, 6, or 7, and all x_i take on the same value, the value of ΔS_{mix} is 1.39R, 1.61R, 1.79R, respectively. The entropic contribution to the free energy at elevated temperatures, T_h , that is, $-T_h \Delta S_{\text{mix}}$, is on the same order as the enthalpy of formation for intermetallic compounds; thereby suppressing their probability of formation. Recent discussions suggest a more nuanced approach in the nomenclature of these new multi-component alloys [25].

Here, the focus is restricted refractory HEAs (RHEAs), which are a promising candidate materials for high temperature structural applications. Several RHEAs have been thoroughly discussed and recently reviewed by Couzinie et al. [26]. These alloys generally exhibit three or fewer phases with a dominate BCC phase[27]. Experimental studies on the high temperature oxidation resistance of RHEAs and the role different

metals play are on-going [28, 29, 30, 31, 32, 33]. Butler and Weaver [28] explored $\text{Al}_x(\text{NiCoCrFe})_{1-x}$ where the Al content was varied. They reported a combination of Al_2O_3 and AlN beneath an external Cr_2O_3 scale across all samples with the general conclusion that increasing Al content improved oxidation resistance by bolstering the position and continuity of the Al_2O_3 scale. Müller et al., [29] studied TaMoCrTiAl , NbMoCrTiAl , NbMoCrAl and TaMoCrAl and reported the formation of a protective oxide layer containing Al_2O_3 , Cr_2O_3 and CrTaO_4 in the quinary Ta-containing alloy with the general conclusion that increased Ta content reduced MoO_3 evaporation and increased oxidation resistance. Schellert et al., [31] performed a similar analysis to [29] on the same HEA where they found a Ta content < 10% resulted in poor oxidation performance. In the computational domain, Taylor et al., [34] reported metal-oxide formation energies calculated with density functional theory (DFT) which suggests Zr, Ta, Nb, Ti, and Al are among the top candidates for oxide resistance with oxide formation energies exceeding 8 eV/atom. Osei-Agyemang and Balasubramanian [35] employed DFT calculations and thermodynamic modeling to study the thermodynamics of oxygen adsorption on the surface of MoWTaTiZr which is among the first applications DFT calculations to study the oxidation of a RHEA surface. They found the surface of MoWTaTiZr to be highly reactive to oxygen with 1 monolayer (ML) oxygen coverage preferred at temperatures 300 K to 1500 K and were unable to recover a clean surface, even at extremely low pressures and high temperatures.

This study examines the surface oxidation of $\text{Al}_{10}\text{Nb}_{15}\text{Ta}_5\text{Ti}_{30}\text{Zr}_{40}$, [36] where oxygen coverage is increased from 0.07 ML to 2 ML on a surface slab generated from a bulk supercell [37, 35]. Here, the solid-phase phase prediction algorithm, $(\text{MC})^2$ [1, 2, 38], was used to predict the bulk structure of the alloy, which is then used to generate candidate surface structures. This is different from previous studies where the phase of the bulk material was assumed and the bulk alloy was generated ran-

domly, rather than from equilibrium. DFT calculations and thermodynamic modeling were performed and stable oxygen coverage over a large scale of temperatures and pressures was examined. Oxygen was systematically adsorbed to the (011) surface using the energetically preferred hollow sites. Affinity towards the different metal atoms is discussed. Charge analysis was executed using the Bader code [39]. Successive adsorption energy as a function of the surface composition and oxygen coverage was generated using the method of least squares. Five (011) surface slabs with differing metallic compositions were explored using the successive adsorption energy function in a Grand Canonical Monte Carlo Simulation (GCMC). Climbing image nudged elastic band (CI-NEB) calculations were employed to calculate the activation energies for five diffusion routes from the top surface layer to the first subsurface layer at low and 1 ML oxygen coverage. This work may help increase our knowledge as to how material properties are affected as the oxidation process occurs. Such properties are typically needed as input for continuum models [37].

3.2 Computational Methods

3.2.1 Bulk Structure

The bulk structure was generated using my implementation of the $(MC)^2$ algorithm (see Chp. I) [1, 2]. The simulation was performed at $T = 1273.15$ K, $P = 0$ Pa, and the five simulation cells were initialized with 32 atoms per cell in initial configurations of BCC, HCP, FCC, BCC, and BCC, where BCC, HCP, and FCC are the body centered cubic, hexagonal close-packed, and face centered cubic crystal structures, respectively. Equilibrium was reached in about 350 steps and was sampled for an additional 1,311 steps for a total run consisting of 1,661 steps.

DFT calculations were performed using the Projector Augmented Wave (PAW) method as implemented by the Vienna Ab-initio Software Package (VASP) [3, 4]. The

calculations were performed with a plane wave cutoff energy of 450 eV and a 2x2x2 Monkhorst-Pack [5] k-point mesh. DFT calculations performed on the simulation cells allowed for changes in the volume and atomic positions through the setting ISIF = 3. The electronic self-consistent calculation was converged to 1×10^{-6} eV and ionic relaxation steps were performed using the conjugate-gradient method (IBRION = 2) and continued until the total force on each atom dropped below a tolerance of 1×10^{-2} eV/Å. The generalized gradient approximation (GGA) was used for the exchange correlation functionals as parameterized by Perdew-Burke and Ernzerof (PBE) [21]. The PAW pseudopotentials [4] were used with the valence electron configurations $3s^23p^1$, $4p^65s^14d^4$, $6s^25d^3$, $3d^34s^1$, and $5s^24d^15p^1$, for Al, Nb, Ta, Ti, and Zr, respectively.

3.2.2 Surface Study

In an effort to keep the number of computations reasonable and reduce the computational overhead, surface slabs were generated from the $(MC)^2$ simulation cell with the largest molar fraction using an in-house code for generating surface slabs. In this case, this corresponded to the 4th simulation cell, a BCC crystal structure with atomic concentrations closely matching that of the RHEA BCC matrix. Initially, one equilibrium bulk configuration was extracted and surface slabs along the (010), (011), and (111) directions were generated using the surface slab tool [9]. The bulk structure and surface cuts are shown in Figure 8. Surface terminations were chosen such that each slab contained all members of the alloy to maximize insight on how the adsorbed oxygen interacts with different members of the alloy. The surface slab with the lowest surface energy was chosen for additional study; for this work it was the (011) slab. Two additional bulk equilibrium configurations of the 4th simulation cell were extracted from $(MC)^2$ and two new (011) surface slabs were generated. The (011) slab with the lowest surface energy was used for the adsorption study. The

surface slabs consisted of 4 layers, 2 to represent the surface, and 2 to represent the bulk, and a vacuum layer of 20 Å along the \hat{c} direction to prohibit interaction between image slabs. Selective dynamics were used to freeze the bulk layers while the surface layers and O-adsorbate(s) were free to move in the \hat{a} , \hat{b} , and \hat{c} directions.

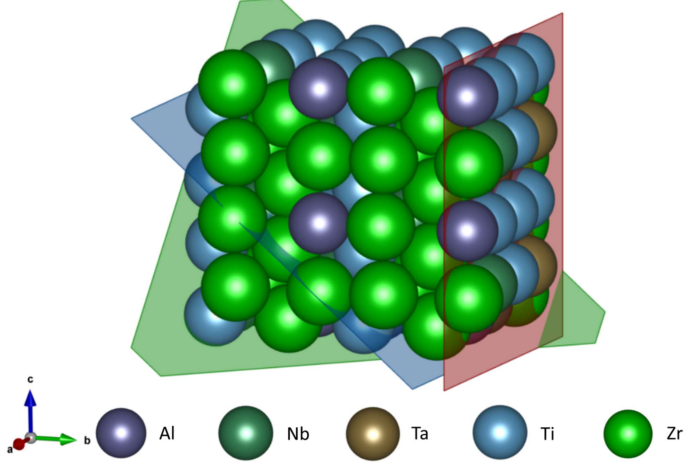


Figure 8. The BCC bulk structure multiplied into a larger supercell for surface cuts. The (010), (011), and (111) surface planes are shown in red, blue, and green, respectively.

DFT calculations were executed with a plane wave cut-off energy of 600 eV and a 3x3x1 Gamma-point-centered Monkhorst-Pack k-point grid [5]. The electronic energy was converged with respect to the k-point grid and energy cut-off to within 1 meV. Through propagation of error in the electronic energies, surface energies were reported with confidence up to 0.1 meV/Å². Electronic relaxation was converged to 1x10⁻⁶ eV and ionic relaxation steps were continued until a force tolerance criterion of 1x10⁻² eV/Å was satisfied. The PAW pseudopotentials had the same valence electron configurations as stated in the previous subsection, with the addition of an electron valence configuration of 2s²2p⁴ for oxygen. The surface energy per area is given by,

$$E_{\text{surf}} = \frac{1}{2A} (E_{\text{slab}} - NE_{\text{bulk}}), \quad (21)$$

where A is the area of the surface slab, in units \AA^2 , E_{slab} is the total energy of the the surface slab, in units of eV, N is the number of atoms present in the surface slab, and E_{bulk} is the energy per atom of the bulk structure from which the surface slab was cut, in units of eV/atom.

Adsorption calculations were executed using an energy cut-off of 600 eV, an electronic relaxation convergence setting of 1×10^{-6} eV, and force tolerance criteria of 1×10^{-2} eV/ \AA . Electronic energies were converged with respect to the k-point grid and plane wave cut-off energy to within 1 meV. Through propagation of error in the electronic energies, the adsorption energies were reported with confidence up to 1 meV. An attempt to activate dipole corrections along the \hat{c} direction was made, but this resulted in poor convergence with the conjugate gradient method (IBRION = 2); therefore it was deactivated. The k-point grid was altered between 1x1x1 and 3x3x1 at different points in the routine and the projection operators were evaluated in real-space through the setting LREAL = Auto, with a final, static, calculation being performed with the projection operators done in reciprocal space. Making coarse measurements (1x1x1, LREAL=Auto) that were later refined (3x3x1, LREAL=.FALSE.) greatly reduced the computational cost of this work. To limit the number of adsorption sites to consider, six adsorption calculations were performed with a single O atom placed at two different on-top, bridge, and hollow sites using a k-point grid of 3x3x1. The O atom was placed 1.75 \AA above the surface for the on-top and bridge sites and 1.25 \AA above the surface for the hollow sites. The 2 on-top and bridge calculations resulted in the O atom displacing to a hollow site and both hollow-placed O atoms remained in the hollow site they were placed. Therefore, only hollow sites were considered when consecutively placing O atoms to increase the coverage.

For every additional O atom placed, two rounds of adsorption calculations were made on the unoccupied hollow sites. The first round was conducted using a k-

point grid of 1x1x1. From the first round, the three hollow sites with the lowest adsorption energies were selected and the second round of adsorption calculations was executed with a 3x3x1 k-point grid for a more accurate energy. The O atom was placed at the site with the lowest adsorption energy. When three or fewer hollow sites remained unoccupied the routine would execute only the 3x3x1 adsorption calculation and choose the minimum from that point. The adsorption and successive adsorption energies are given by,

$$E_{\text{ads}} = \left(E_{\text{slab}}^{\text{O}(n)} - E_{\text{slab}} - \frac{n}{2} E_{\text{O}_2} \right) \quad (22)$$

$$E_{\text{ads}}^{\text{Succ}} = \left(E_{\text{slab}}^{\text{O}(n+1)} - E_{\text{slab}}^{\text{O}(n)} - \frac{1}{2} E_{\text{O}_2} \right) \quad (23)$$

where $E_{\text{slab}}^{\text{O}(n)}$ is the total electronic energy of the oxidized slab, E_{slab} is the total electronic energy of the clean slab, n is the number of O atoms present, E_{O_2} is the energy of the gas phase O_2 molecule, and $E_{\text{slab}}^{\text{O}(n+1)} - E_{\text{slab}}^{\text{O}(n)}$ is the difference in electronic energy between the surface with n O-atoms and $n + 1$ O-atoms present. The binding energy of O_2 was calculated by placing two O atoms in a box of dimensions (8, 8, 8) Å separated along the \hat{c} direction by 1.22 Å. The calculated binding energy was -9.86 eV. The surface slab coverage was increased from 1/15 monolayer (ML) to 15/15 ML using a step of 1/15 ML. Once full coverage was achieved, a 16th O atom was introduced to the fully covered surface slab. The 16th O atom was restricted to move only in the \hat{c} direction to avoid adsorption at top layer bridge sites. The 16th adsorption event occurred at the site where the first O atom was adsorbed and caused the O atom which already occupied this site to move in the $-\hat{c}$ direction to the first subsurface layer. The original O atom diffused below the hollow site it previously occupied, on-top of Zr, surrounded by 3 Ti and 1 Zr. This event had a successive adsorption energy of $E_{\text{ads}}^{\text{Succ}} = -2.606$ eV, a value larger than the largest first-layer adsorption event by 1.518 eV. This positive difference in adsorption energy demonstrates that an

O-O repulsion event which results in O diffusing to the subsurface will not occur until all adsorption sites are occupied. The monolayer study was resumed from the 15/15 ML surface structure, where O atoms were introduced to hollow adsorption sites on the first subsurface layer. The same routine to progress from 1/15 to 15/15 ML was performed to progress from 16/15 to 30/15 ML coverage at a step of 1/15 ML. Once finished, the work function was calculated for the clean slab up to the 30/15 ML oxygen coverage.

The Bader algorithm [39] was used to examine the charge transfer between the surface slab and O-atoms. Using the clean surface slab as the point of reference, the charge transferred is defined as,

$$\Delta q_j = q_{i,0} - q_{i,j}, \quad (24)$$

where j indexes the ML structure, and i indexes the alloy atoms in the surface slab, not to include the oxygen, and $q_{i,0}$ is the charge value of atom i in the clean surface. The result is a matrix of charge transfer which catalogues the difference of each atom's charge at each ML structure in reference to its initial charge value. As it is defined in Eq. 24, a positive Δq value indicates a gain of electrons.

The Gibbs free energy of formation per atom was calculated for the coverage configurations using the following expression,

$$\Delta G = \left((E_{\text{slab}}^{\text{O(n)}} + F_{\text{vib}}) - E_{\text{slab}} - n\mu_{\text{O}}(T, P) - TS_{\text{mix}} \right) / (N + n) \quad (25)$$

where $E_{\text{slab}}^{\text{O(n)}}$ is the total electronic energy of the oxidized slab, E_{slab} is the total electronic energy of the clean slab, N is the number of metal atoms, and n is the number of O atoms present. F_{vib} refers to the Helmholtz vibrational energy and is a function of temperature and phonon frequency. The expression for the Helmholtz

vibrational energy, within the harmonic approximation, is given as,

$$F_{\text{vib}} = -k_B T \ln(Z) = \frac{1}{2} \sum_{\mathbf{q}j}^{3n} \hbar \omega_j(\mathbf{q}) + k_B T \sum_{\mathbf{q}j}^{3n} \ln [1 - \exp(-\hbar \omega_j(\mathbf{q})/k_B T)], \quad (26)$$

where Z is the vibrational partition function, and the number of normal modes, or frequencies, is equal to the number of O atoms present in the system, n , multiplied by the number of degrees of freedom, i.e. $3n$ normal modes. The phonon frequencies for point \vec{q} in the first Brillouin Zone and band index j , $\omega_j(\mathbf{q})$, were calculated using the finite-difference method as implemented by VASP (IBIRON = 5) with Γ -point sampling only. The term μ_O represents the chemical potential of oxygen and is expressed as,

$$\mu_O(T, P_{O_2}) = \frac{1}{2} E_{O_2} + \Delta \mu_O(T, P_{O_2}). \quad (27)$$

The first term in Eq. 38 is the energy of the gas phase O_2 molecule plus the correction value, ~ 2.3 eV. The second term, $\Delta \mu_O$ is a correction term which is treated as a parameter and is expressed as,

$$\Delta \mu_O(T, P_{O_2}) = \frac{1}{2} \left(\mu_{O_2}^0 + k_B T \ln \left(\frac{P_{O_2}}{P^0} \right) \right). \quad (28)$$

The term $\mu_{O_2}^0$ in Eq. 39 is the difference of the chemical potential of O_2 at $T = 0$ K and $T > 0$ K under $P = 1$ atm and can be calculated at different temperatures, while holding the pressure constant, using the Joint Army-Navy-Air Force (JANAF) tables [40] as demonstrated in [41, 42]. The entropy of mixing term, S_{mix} , in Eq. 37 is defined in Eq. 40 and is a constant value in this case, because the atomic concentrations of each species, x_i , are unchanged.

$$S_{\text{mix}} = -k_B \sum_{i=1}^5 x_i \ln(x_i) \quad (29)$$

For this study, P^0 was set to 1 bar and the system was analyzed in the temperature and pressure ranges of [100 K, 2600 K], [10^{-30} bar, 10^5 bar], respectively. For each set of (T,P) the coverage with the lowest Gibbs free energy was identified and a stability plot was produced. The temperature bin width for the stability plot is 100 K and was restricted to that of the JANAF tables. The pressure range was divided into 35,000 data points; a finer division was tested, but led to negligible improvements. For a given temperature, the Gibbs free energy was calculated for each of the 35,000 pressures. Then, the list of energies was scanned and the coverage with the lowest Gibbs energy at each pressure value was recorded.

Using the surface adsorption study results, a least squares generated function was derived for the successive adsorption energy as a function of the number of metal and oxygen atoms present within a cutoff radius of 3.5 Å of the adsorption site; this included first and second surface layer atoms at some sites. A linear function form was assumed,

$$E_{\text{ads}}^{\text{Succ}}(\mathbf{n}, n_{\text{O}}) = an_{\text{Al}} + bn_{\text{Nb}} + cn_{\text{Ta}} + dn_{\text{Ti}} + en_{\text{Zr}} + fn_{\text{O}}$$

where a, b, c, d, e, f are coefficients found using the method of least squares, \mathbf{n} is the number of each metal atom in the slab, and n_{O} is the number of O atoms present on the slab. The coefficient values and a parity plot has been provided in Appendix A. The matrix elements, $a_{i,j}$, represent the number of metal atom type j present at adsorption site i . The coefficients were stored in a coefficient vector, \mathbf{w} . For different terminations of the (011) slab an \mathbf{A} matrix can be generated and operated on \mathbf{w} to yield the successive adsorption energies expected on that slab. The successive adsorption energies for three new configurations of the original (011) slab at 1 ML were used in a Grand Canonical Monte Carlo (GCMC) simulation where two moves were attempted, oxygen insertion and oxygen deletion, whose acceptance probabilities

are given in Eq. 30 and 31.

$$P_{\text{accept}}^{\text{insert}} = \min \left\{ 1, \frac{V}{\Lambda^3(N+1)} \exp(\beta\mu) \exp(-\beta\Delta U) \right\} \quad (30)$$

$$P_{\text{accept}}^{\text{delete}} = \min \left\{ 1, \frac{\Lambda^3 N}{V} \exp(-\beta\mu) \exp(-\beta\Delta U) \right\} \quad (31)$$

In Eqs. 30 and 31, V is the simulation cell volume, Λ is the thermal de Broglie wavelength, N is the number of atoms present, metals and oxygen, $\beta = 1/k_B T$ where k_B is the Boltzmann constant, T is temperature, μ is the oxygen chemical potential given in Eq. 38, and ΔU is the energy difference which is given in Eq. 32,

$$\Delta U = E_{\text{ads}}^{\text{Succ}} + \frac{1}{2} E_{\text{O}_2}. \quad (32)$$

The temperature domain was swept from 100 K to 2600 K with a step of 100 K, the pressure domain was swept from 10^{-30} bar to 10^5 bar with a step of 10^3 bar and a stability plot was generated up to 1 ML. Each GCMC simulation was executed for 5,000 steps. To examine the impact of each species contribution to the oxidation resistance, 8 Zr atoms present on either the first or second layer were flipped to Al, Nb, and Ti in slabs II, III, and IV, respectively, as shown in Figure 9. Because Ta was scarce on the training slab, fluctuations in Ta content was not explored.

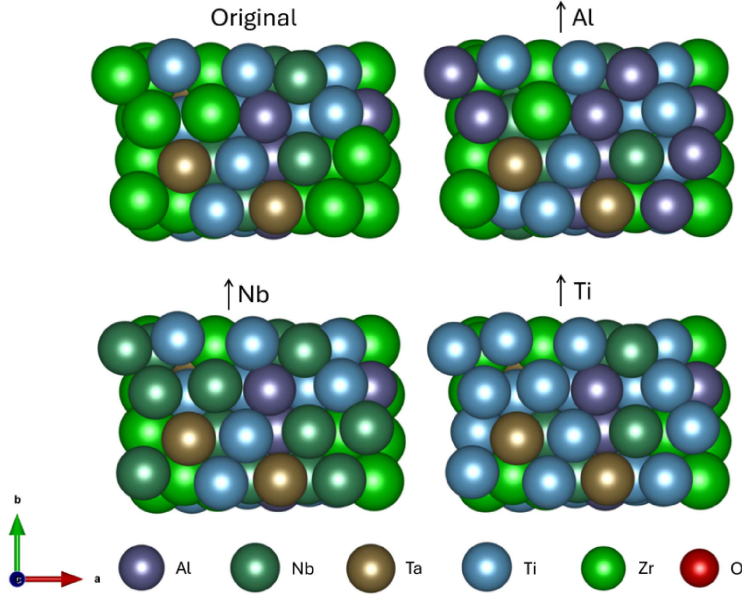


Figure 9. The final configuration of the original (011) surface slab at 1 ML shown against the slabs that were enhanced in Al, Nb, and Ti content, labeled accordingly.

The energy barrier for an O atom to diffuse from the top surface layer to the first subsurface layer was calculated using the climbing image nudged elastic band (CI-NEB) method [43] as implemented by the software VASP Transition State Theory (VTST). The calculation was carried out using six images and a spring constant of -5.0 eV/ \AA^2 . The initial and final positions were completely relaxed before calling the CI-NEB calculations. The initial configuration for each of the five sites is shown, as seen in VESTA, in Figure 10. Site I, II, and III were also analyzed at 1 ML coverage to examine diffusion at high coverage. The convergence parameters remained unchanged from the previous VASP calculations and a k-point density of 3x3x1 was used.

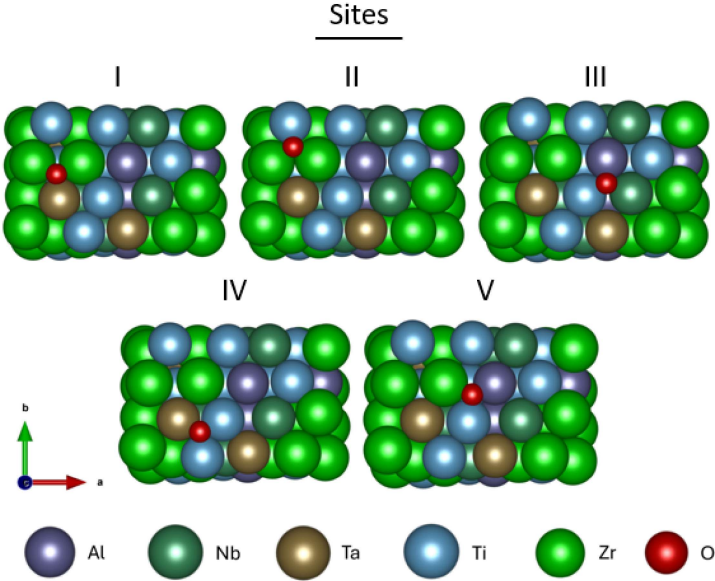


Figure 10. The initial slab configuration for the five diffusion events

3.3 Results & Discussion

$(MC)^2$ predicts a majority phase, with a molar fraction of $86.84 \pm 2.44\%$, at the composition of the BCC matrix, $Al_9Nb_{16}Ta_3Ti_{31}Zr_{41}$, within the RHEA at 1273.15 K, $P = 0$ bar, which agrees with the experimentally observed single BCC phase seen at $T = 1373.15$ K. The final results of the $(MC)^2$ algorithm are reported in Table 2, where the averaged values were calculated using the data from MC step 350 and onward. The fidelity of the At.% values are 0.03125, or $1/32$. To reduce this value, and therefore increase the precision of the predictions, more atoms need to be included in the simulation cells. When using a software like VASP, doing so greatly increases the cost of the simulation. Figure 11 shows the progression of each phase, or simulation cell's, molar fraction value versus MC step. The vertical solid black line is placed approximately where the simulation enters equilibrium, around 350 steps.

Table 2. Simulation results for generating the bulk structure using $(MC)^2$

		Cell Name				
		1	2	3	4	5
Cell	Initial	BCC	HCP	FCC	BCC	BCC
Structure	Final	HCP	HCP	FCC	BCC	BCC
Molar Fraction	Average	0.0263	0.0368	0.0579	0.8684	0.0105
Fraction	Stdev	0.0125	0.0110	0.0244	0.0210	0.0173
		At.%				
Majority Phase		Al	Nb	Ta	Ti	Zr
Cell 4	Final	9.375	15.625	3.125	31.25	40.625

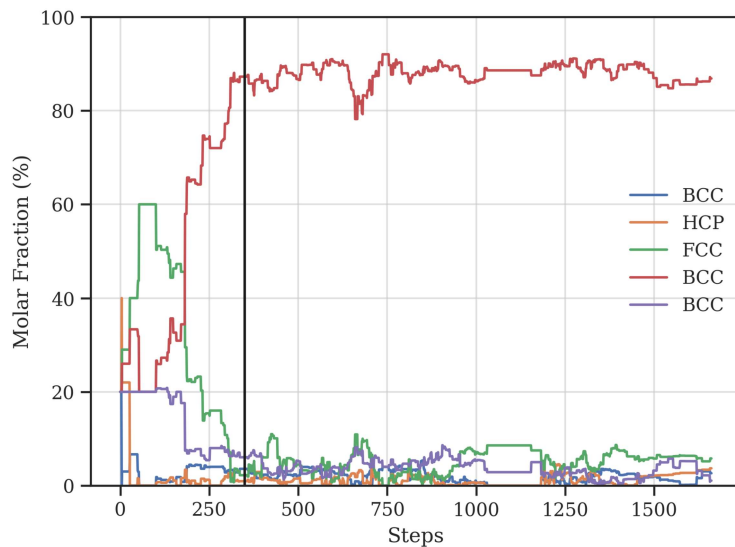


Figure 11. The molar fraction value plotted against the MC step for the five simulation cells. Equilibrium begins approximately where the solid vertical line is drawn.

Table 3 shows the lattice constant for each of the three equilibrium BCC bulk structures, as well as, the average lattice constant, 3.402 \AA , whose value is in excellent agreement with the experimentally measured lattice constant of 3.401 \AA , with a percent error value of 0.03%. Figure 12 (a) shows the projected density of states

(DOS) for the BCC Configuration I. Figure 12 (b) is a histogram which shows each species distribution of states over the s-, p-, and d-orbitals. Ti and Zr have a high number of d-orbital states in the conduction band and near the Fermi level which leads to a strong interaction between O and these species.

Table 3. Lattice constants and angles of the three BCC equilibrium structures considered in this study.

BCC Phase	a_0	α	β	γ
Config I	3.400	89.86	89.84	90.90
Config II	3.403	89.90	89.96	90.92
Config III	3.404	90.12	89.73	91.01
Average	3.402	89.96	89.84	90.94

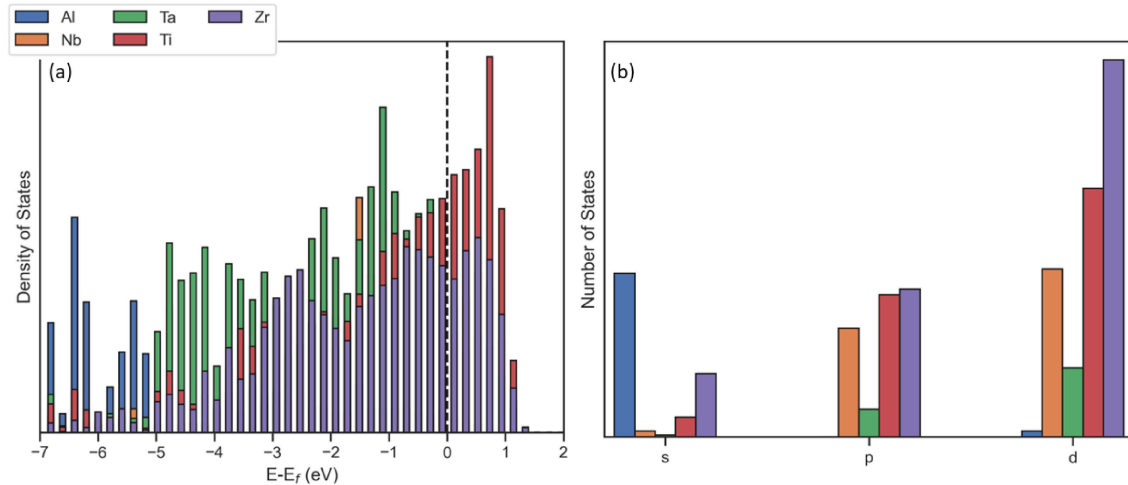


Figure 12. (a) The projected density of states for BCC Configuration I. (b) State distribution over the s-, p-, and d-orbitals.

The surface energy for the (010), (011), and (111) were 122.0, 110.6, and 121.3 meV/ \AA^2 , respectively. The additional (011) surface slab energies varied by about 1 meV/ \AA^2 . The (011) surface slab used in the oxygen adsorption study is shown, as seen in VESTA, in Figure 13 and had the lowest surface energy out of the three (011) configurations.

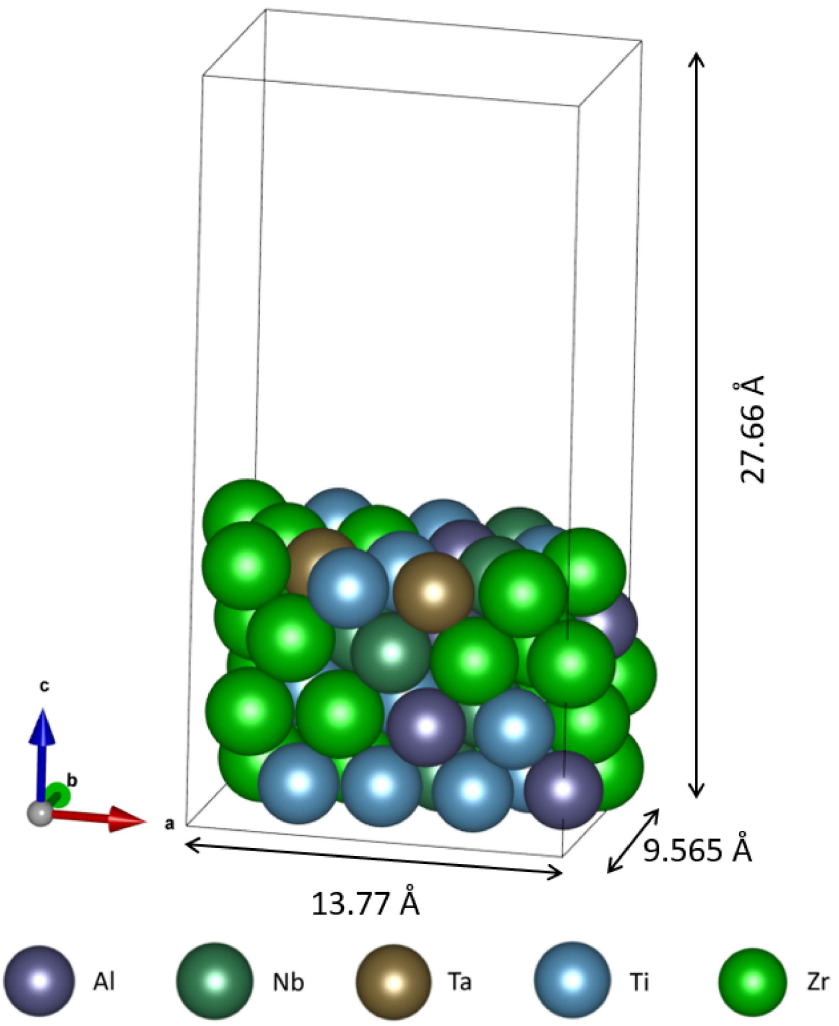


Figure 13. The (011) surface slab generated from the body centered cubic bulk structure

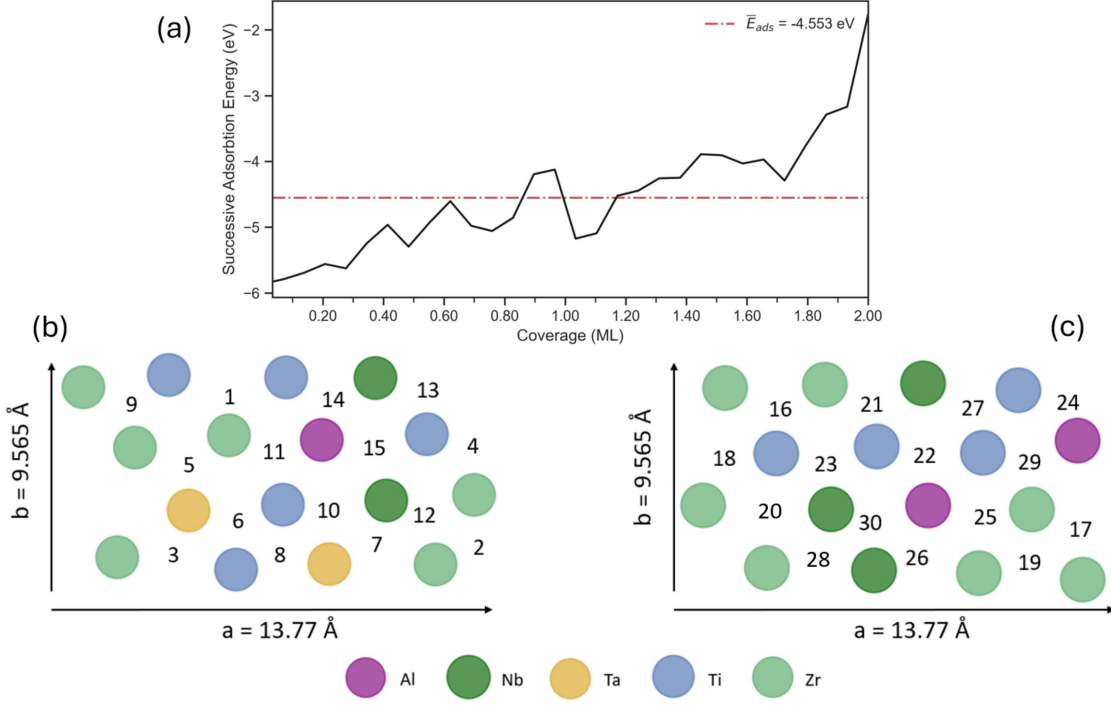


Figure 14. (a) Successive adsorption energy plotted against the coverage. (b) The top-most layer of the surface slab with each adsorption event labeled in order from 1st to 15th O atom adsorbed. (c) The second surface layer with each adsorption event labeled in order from 16th to 30th O atom adsorbed.

Figure 14 (a) shows the successive adsorption energy versus coverage, (b) is the top surface layer with the order of oxygen adsorption labeled, and (c) is the second surface layer with the order of oxygen adsorption labeled. The successive adsorption energy varies as sites with different metallic combinations are explored. Sites with Ti and Zr present corresponded to a decrease in adsorption energy on both surface layers, indicating that the presence of Ti and Zr increased the likelihood of oxygen adsorption to that site. Adsorption to sites with Nb present resulted in an increase in adsorption energy, especially in the absence of Ti and Zr. Adsorption to a site where the combination of Nb/Al and Nb/Ta was present resulted in a large increase in adsorption energy. The general upward trend of successive adsorption energy is contributed to increased O-O repulsion as neighboring sites became occupied. A strong case of this was seen at the 30th adsorption event, where O-O repulsion forces

the final oxygen to settle at a bridge adsorption site, which in turns pushes a neighboring O atom atop Zr. Referring to Figure 12, the preferential adsorption by O to sites with Ti and Zr is explained by the strong covalent bonds formed as a result of the unfilled d-orbitals of Zr and Ti. Preferential adsorption to sites with Zr and Ti was also reported by a similar first-principles HEA oxidation study [35]. Adsorption energy per adsorbate is shown in Figure 15. While adsorption energy does increase with increasing oxygen coverage, it remains favorable up to 2 ML, and likely beyond.

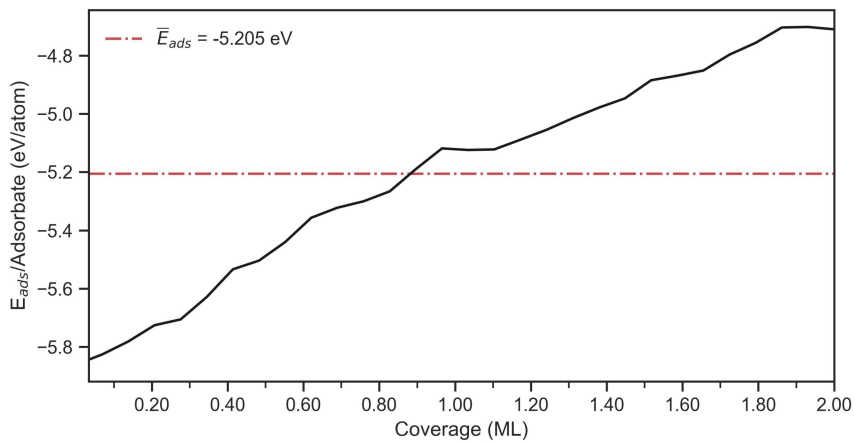


Figure 15. Adsorption energy per adsorbate versus oxygen coverage

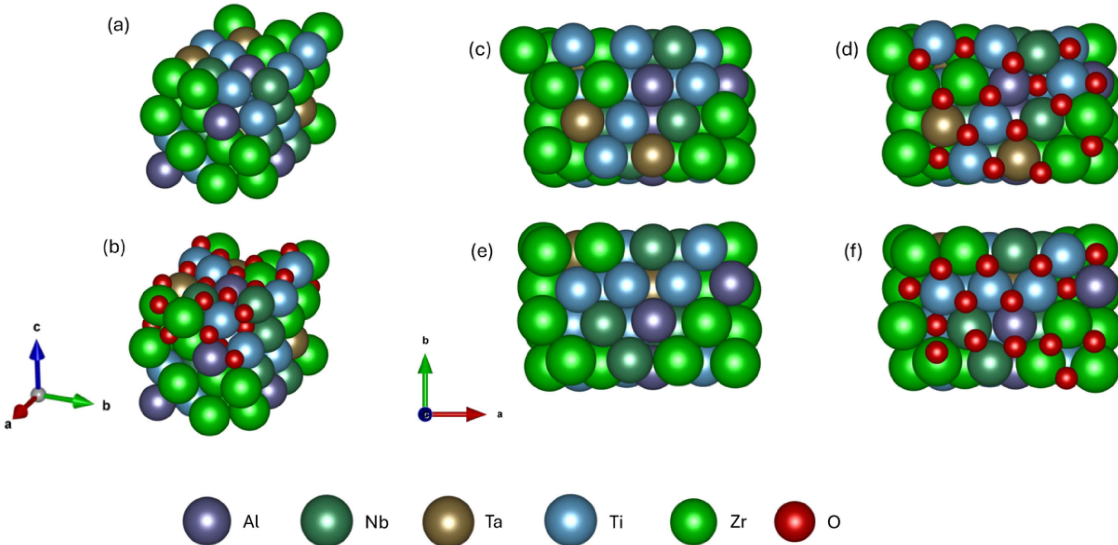


Figure 16. (a) Full view of the initial (011) surface slab. (b) Full view of the surface slab at 2 ML. (c) The first surface layer at 0 ML. (d) the first surface layer at 1 ML. (e) The second surface layer at 0 ML. (f) The second surface layer at 2 ML.

The final configuration of the surface slab is shown in Figure 16, where (a) and (b) shows the initial and final surface structure, (c) and (d) shows the top surface layer at 0 ML and 1 ML, and (e) and (f) shows the second surface layer at 0 ML and 2 ML. The distance between the first and second layer increased by 0.5 Å, while the distance between the first bulk layer and second surface layer saw a negligible increase. Second layer surface atom positions were largely unperturbed as coverage on the top surface layer was increased. Increasing the oxygen coverage from 1 ML to 2 ML led to inward movement of two top surface Ta atoms, and a top surface Zr and Ti atom.

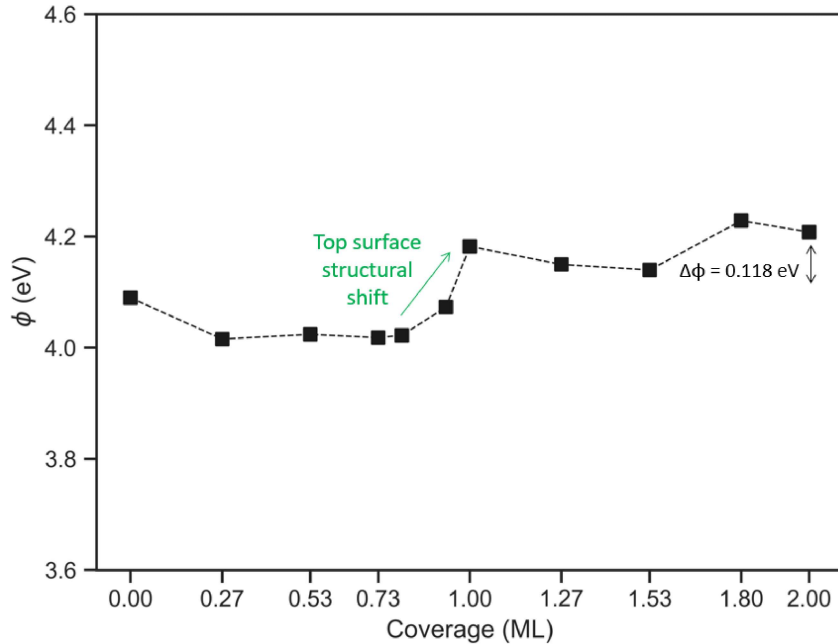


Figure 17. The work function value over increasing coverage

The work function was calculated using the expression, $\phi = E_{\text{vac}} - E_F$, where E_{vac} is found from the averaged electrostatic potential and E_F is the Fermi energy. Figure 17 shows ϕ against the oxygen coverage. The work function decreases until 0.27 ML where it remained fairly constant until a large increase around 0.80 ML. A comparison between the structure at 0.80 ML, 0.93 ML, and 1.00 ML showed a large displacement of Al by the 15th O atom, pushing Zr and Al together. The change in surface structure is a good candidate behind the boost in work function. The work function is relatively constant from 1.00 ML to 2.00 ML. The difference in the work function between clean and 2.00 ML was 0.118 eV. An increase in work function can be explained by the change in electrostatic dipole moment [44] as charge is transferred from the metal surface to the O atoms; the shift of the surface is to a more positive state, while the O atoms become more negative, and this influences the work function. A decrease in value indicates the alloy has a weaker bind on its electrons, making oxygen binding more thermodynamically favorable. Hugosson et

al., [45] reported an increase in the work function as oxygen coverage increased on the (001) surface of iron. Huber and Kirk [46] observed the reduction of the Al work function as oxygen coverage increased. A similar study to this was conducted by Guo et al., [47] on the pure Ta surface where they reported negligible changes in the work function vs. coverage on the (110) face. The mixture of five different metals on the surface leads to a more complicated behavior in the work function.

The average M-O bond lengths at the first and second surface layer are reported in Table 4. The M-O bond length was shorter at the second layer; indicating the formation of stronger bonds. When comparing the M-O bonds at low versus high oxygen coverage, it was found that bond length decreased with increasing O population.

Table 4. Average bond length for M-O compounds measured on the 2 ML surface slab

M-O	Top (Å)	Subsurface (Å)	Ref (Å)
Al	1.96	1.86	1.85, 1.96 [48]
Nb	2.17	2.08	2.195, 2.290 [49]
Ta	2.27	2.06	1.98[50], 2.33[47]
Ti	2.09	1.97	1.832, 2.229 [51]
Zr	2.26	2.14	2.25 [52]

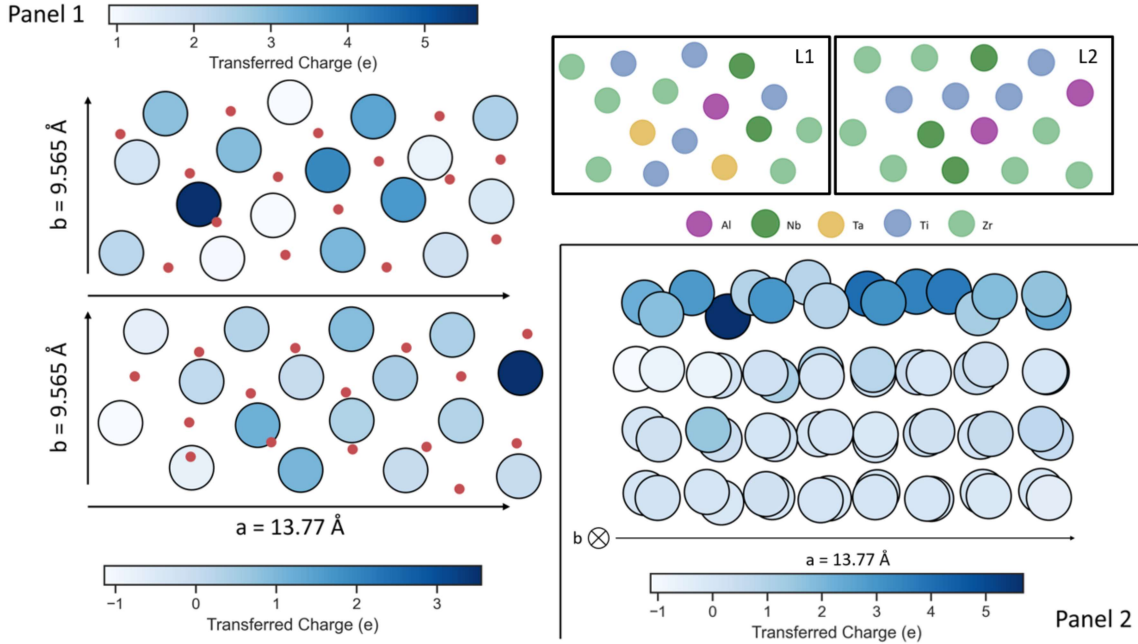


Figure 18. (Panel 1) The charge transferred by members of surface layer 1, (Top Left), and surface layer 2, (Bottom Left), under 1 ML and 2 ML coverage. Two site maps of surface layer 1 and 2 have been included in the upper right corner of Panel 1 to help readers identify which members occupy which positions. (Panel 2) A side view, where b points into the page, of the surface slab showing how charge is transferred as a function of depth.

The results from the Bader charge analysis are shown in Figure 18, where the first and second surface layer, referred to as L1 and L2 respectively, are displayed under full coverage, 1.00 ML and 2.00 ML, in (Panel 1). To help identify which alloy species occupies which site in the transferred charge plots, a site map of L1 and L2 has been included in the upper right corner of (Panel 1). Figure 18 (Panel 2) shows the transferred charge between the four layers of the surface slab. Beginning with (Panel 1), the strongest transfer of charge to the O atom in L1 is from the Ta and Al, followed by Nb, Ti, and Zr. The strong donation of charge by Ta is consistent with the first-principles investigation of oxidation on the pure Ta surface by Guo et al.[47]. In L2, the highest transfer is from Al followed by Nb, Ti, and Zr. Note the difference in the L1 and L2 heat map values, the strongest charge interaction occurs between the O atoms and L1. This is further supported in the layer-by-layer comparison shown

in (Panel 2) where the highest amount of charge, darkest color, is seen in L1. The donation of charge from Nb to O is in support of the experimental observation that Nb near the surface discouraged outward diffusion of metal cations [30]. Its charge transfer to O leaves it more positively charged, leading to the repulsion of cations.

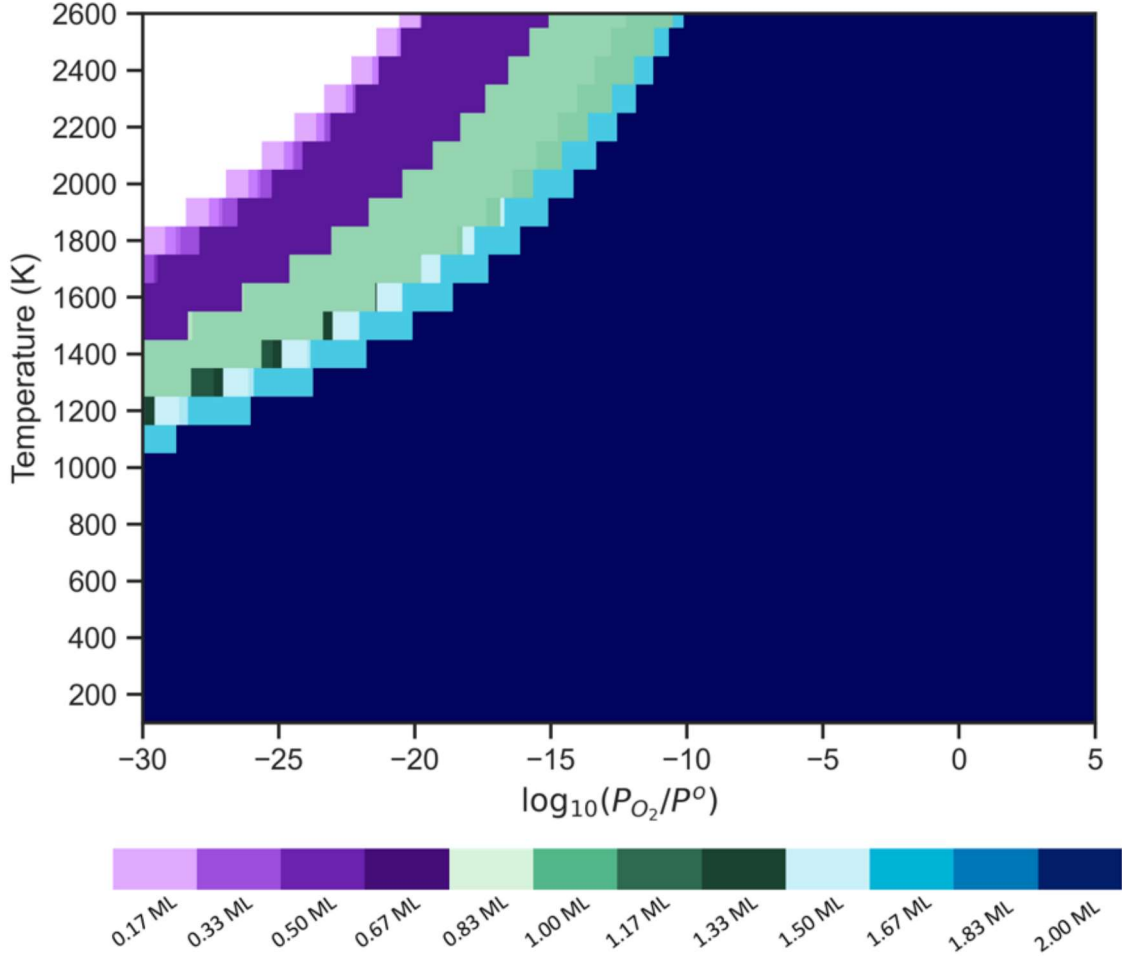


Figure 19. The stability plot which was generated using the results of the thermodynamics study. Extreme temperatures and pressures were considered only for academic purposes. The shading has been assigned to indicate increasing coverage, where white represents the clean surface, purples represent low coverage, greens represent moderate coverage, and blues represents high coverage.

Figure 19 is the key output from the thermodynamics study. Removal of oxygen from the the (011) surface of $Al_9Nb_{16}Ta_3Ti_{31}Zr_{41}$ was not possible under realistic conditions and 2.00 ML is the thermodynamically stable oxygen coverage over the

domain of operational possibilities. This is in good agreement behavior reported by Osei-Agyemang and Balasubramanian [35] where a systematic investigation of oxygen adsorption on a HEA surface up to 1 ML revealed a strong affinity for oxygen, even at pressures as low as 10^{-9} bar and temperatures as high as 2000 K. The investigation to such extreme pressures was purely academic as I wished to identify the set of {T,P} values where the clean slab is preferred. A clean (011) surface was recovered at $P < 1 \times 10^{-18}$ bar and $T > 1900$ K.

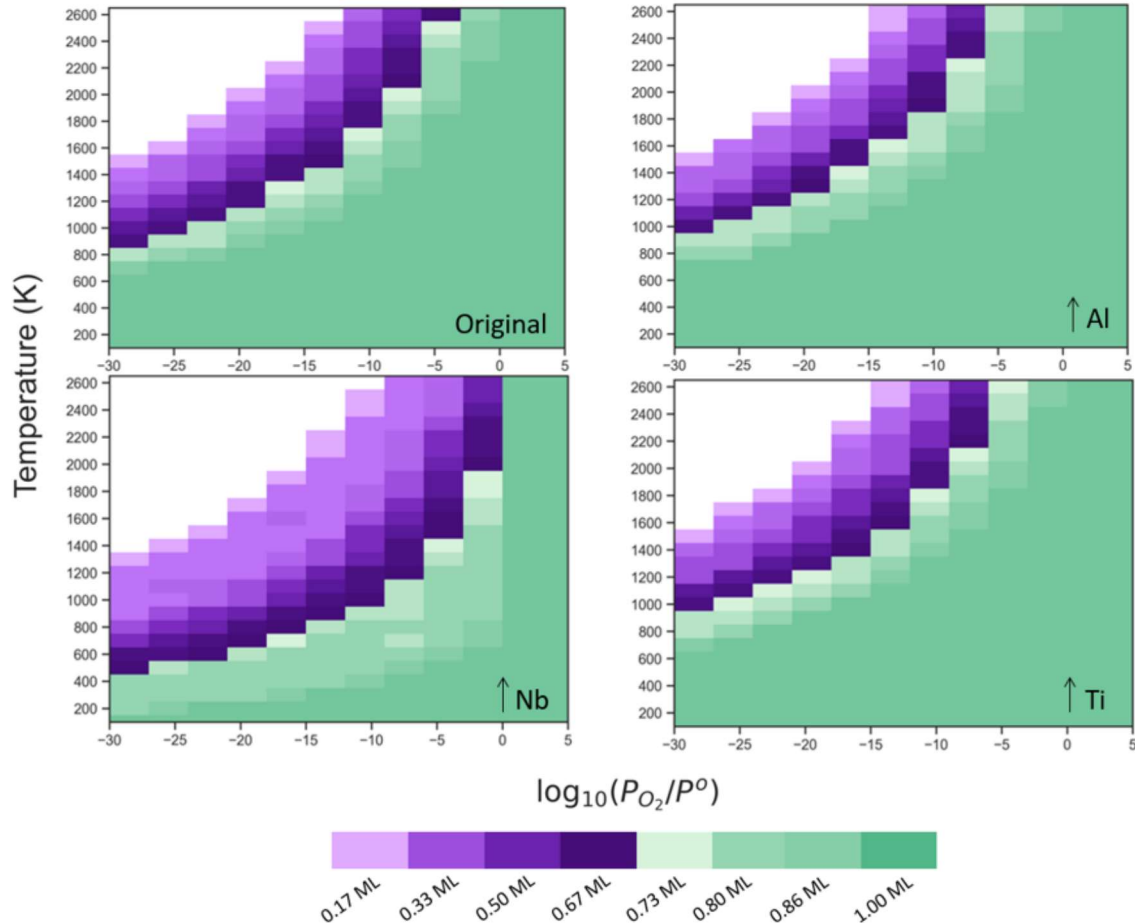


Figure 20. Stability plots generated using the successive adsorption energy function with a GCMC simulation for the original slab, and a slab with increased Al, Nb, and Ti content, labeled respectively. The shading has been assigned to indicate increasing coverage, where white represents the clean surface, purples represent low to moderate coverage, and greens represent high to full coverage.

The compilation of the GCMC results is shown in Figure 20, where the stability

plot of the original surface slab is shown against the stability plot of the slab with increased Al, Nb, and Ti content on the first and second surface, labeled accordingly. The addition of Al and Ti had a negligible impact on the oxidation resistance. Increasing the presence of Nb at the surface increased the oxidation resistance; this can be visualized by the increase in area of the “clean” region, represented in white, in the stability plot. This result is in good agreement with the behavior reported in the adsorption study, where adsorption sites with Nb resulted in an increased successive adsorption energy.

Table 5 shows the results of the CI-NEB study and Figure 21 shows the energetic pathway plotted against the reaction coordinate, movement in the $-\hat{c}$ direction in this case. The **Metal** category in Table 5 lists what metal atoms were present at the initial site. Site I investigated the diffusion from a top layer hollow site with 2 Zr, 1 Ta to a second layer pseudo-stable bridge site between a Zr and Ti. Site II was the diffusion from a top layer hollow site with 2 Zr and 1 Ti to a second layer hollow site with 2 Zr and 1 Ti. Site III was the diffusion from a top layer hollow site with 1 Al, 1 Ti, and 1 Nb to a second layer hollow site with 2 Ti and 1 Al. Site IV was the diffusion from a top layer hollow site with 2 Ti and 1 Ta to a second layer hollow site with 1 Zr and 2 Nb. Site V was the diffusion from a top layer hollow site with 1 Al, 1 Ti, and 1 Zr to a second layer hollow site with 1 Al, 1 Nb, and 1 Ti. Sites where Zr was present had the lowest activation energies. Comparing Site I against Site II and V, diffusion at Zr-sites was slowed in the presence of Ti and Al. In fact, the highest single-oxygen adsorption route was at Site IV, which has the highest Ti content. Sites with Al present exhibited higher activation energies, as well. While only five sites were considered, the preliminary result is that diffusion inward is preferred in regions rich with Zr, but can be discouraged with the addition of Ti and Al.

Table 5. Results from the CI-NEB calculations

Site	Activation Energy (eV)	Metal
I	1.38	Ta, Zr ₂
1ML	4.44	
II	2.86	Ti, Zr ₂
1ML	9.69	
III	3.39	Al, Nb, Ti
1ML	6.46	
IV	5.22	Ta, Ti ₂
V	3.40	Al, Ti, Zr

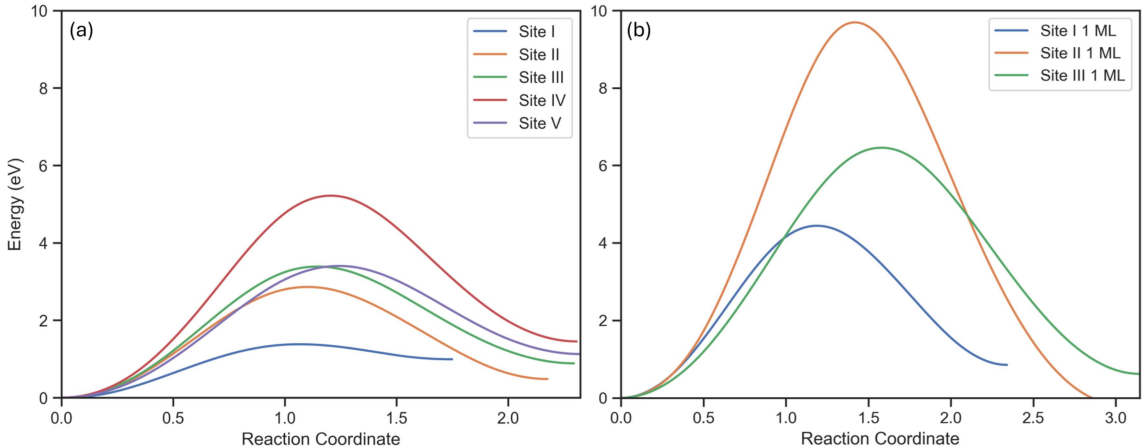


Figure 21. (a) The reaction pathway for the five diffusion sites at low coverage. (b) The reaction pathway for Site I, II, III at 1 ML coverage.

Increasing oxygen coverage to 1 ML reduced the diffusion rates at Sites I, II, III. The increase in activation energy seems to be correlated to the increased rigidity of the top surface layer once multiple oxygen atoms are present and tightly bound to the metal atoms. At Site I, the second surface bridge site the O diffused to at low coverage was no longer accessible. At low coverage, a top layer Zr moved in response to the Site I O atom diffusion. At 1 ML, that Zr is bound to two additional O atoms

and does not reveal the bridge site, see Figure 22. The strong M-O bonds were also responsible for the large increase in activation at Site II, where the neighboring 2 Zr and 1 Ti are tightly bound to 2 additional O atoms. Similar results were seen with Site 3. The preliminary conclusion is that diffusion inward is slowed as coverage increases, where strong M-O bonds prohibit large structural changes that would allow inward migration of O.

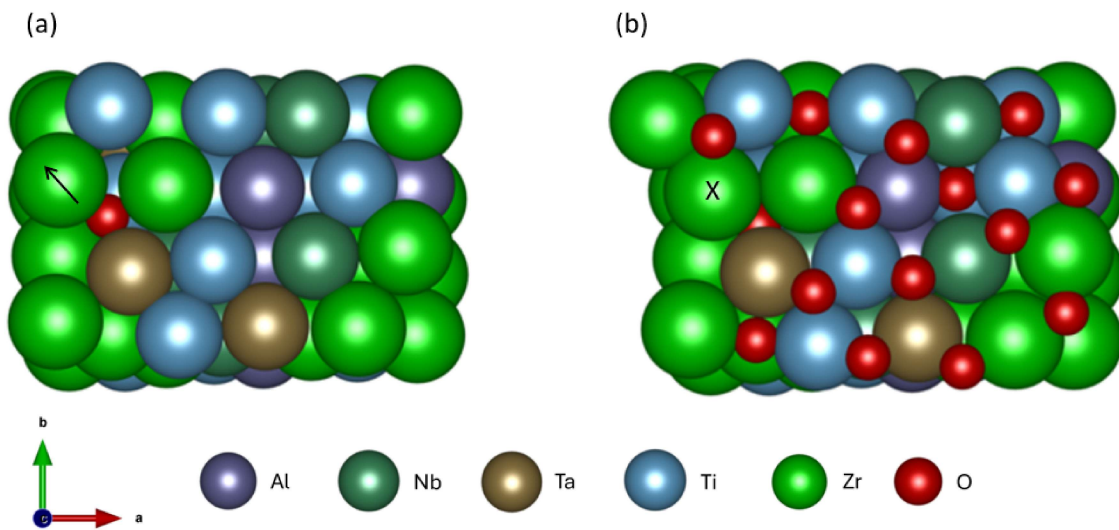


Figure 22. (a) Site I final position with one oxygen present on the surface. (b) Site I final position of 1 ML. An arrow is provided in (a) to indicate the direction the Zr moved in response to the O diffusion. This movement did not take place at 1 ML.

The findings of this work are consistent with experimental observations and may help provide insight about the mechanisms behind these observations from a thermodynamic and kinetic point of view. The results of this work may assist in understanding and predicting the complex oxidation behavior of RHEAs. However, no scientific study is without limitations. (MC)² was executed with simulation cells consisting of 32 atoms, restricting the fidelity at which the compositional domain of the structure was scanned and limiting the ability to comment on the large-scale structure of the material. Smaller cells are also more susceptible to finite size effects. Surface analysis was performed on one (011) surface structure. Behaviors reported here should not

be generalized to what may occur on the {100} and {111} family of surfaces. A more thorough investigation should include results observed on representations from the three surface families. Vibrational corrections were applied to O atoms only and under the harmonic approximation. Including the vibrational contributions of the metal atoms and the vibrational anharmonic corrections were not considered and may have played an important role under certain conditions. The method used to generate the successive adsorption energy function is rudimentary when compared to previously reported models [53, 54], as these account for first and second nearest neighbor interactions, as well as, three and four body interactions. The kinetics of oxygen diffusion was only mildly examined here. A more thorough study would examine diffusion inward from a multitude of different routes with different metal atoms present at the initial and final position and at different oxygen coverage.

3.4 Conclusion

This work examined several aspects of the Al₁₀Nb₁₅Ta₅Ti₃₀Zr₄₀ RHEA. First, (MC)² predicted a single-phase BCC structure at 1,000°C with a lattice constant of 3.402 Å which is in good agreement with experiment. Oxygen strongly favored adsorption sites where Zr and Ti were present and avoided sites where Nb was present. The work function increased with increasing oxygen coverage. M-O bond length decreased as coverage increased, which increased the rigidity of the two surface layers. Charge transferred to the oxygen was most prominent at the top surface layer where Ta, Al, and Nb were the strongest donors in the alloy. The (011) surface was found to be highly reactive with oxygen, with 2 ML coverage dominating the majority of the (T,P) domain studied in the stability plot. The GCMC simulation showed that increasing Nb content at the surface increased the early-stage oxidation resistance. In general, diffusion inward was shown to slow with increased amounts of Ti. Diffusion to

the second surface layer preferred regions rich in Zr, but was slowed with the addition Ti and Al. Inward diffusion at 1 ML coverage was drastically reduced, especially in a region rich with Ti and Zr, which could be due to the strong M-O bonds that formed at an oxygen coverage of 1 ML. Before results can be generalized on how each metal species impacts the early-stage oxidation resistance of this RHEA, more calculations need to be executed to explore the relationship between oxygen and the five metal atoms present on the surface slab.

IV. Chlorine corrosion of a Ni-superalloy

4.1 Introduction

A fundamental understanding of material evolution in corrosive, high temperature, environments is paramount to the field of sustainable energy [55]. Technologies in this field depend on a fluid to manage the heat produced and used within the system. Candidate fluids for these applications are molten halide salts, whose thermal properties, such as boiling point, thermal conductivity, and specific heat, are well suited for the operational environment, where $T > 700^{\circ}\text{C}$ [56, 57]. Of these molten salts, chloride salts are gaining in popularity due to their low cost, low viscosities, and the elimination of the formation of hydrofluoric acid [58]. More specifically, KCl-MgCl₂ is an attractive chloride salt due to its high volumetric heat capacity at 700°C, 0.46 cal/cm³ - °C [58] and is a proposed coolant for molten salt reactor (MSR) designs. Under the U.S. Department of Energy (DOE) Advanced Reactor Demonstration Program (ARDP) several MSR systems are being developed and explored. Two such systems include TerraPower's molten chloride fast reactor (2016) and Southern Company's Molten Chloride Reactor Experiment (MCRE) in association with TerraPower (2020). Some of the many beneficial features of MSRs over other reactor designs include a low-pressure operation, more efficient power conversion, passive heat rejection, and the elimination of solid fuel and the resulting need to build and dispose of it.

One primary issue with MSRs is the corrosion of the salt-facing structural material. At elevated temperatures, corrosion is driven by thermodynamic dissolution of metal-salt compounds into the molten salt coolant [59, 60, 61]. Nickel-based superalloys are candidate alloys due to their good high temperature creep strength and resistance to the corrosive mechanisms encountered in the extreme environments of

MSR systems [62, 63, 64, 65, 66]. The redox potentials for common alloying elements in decreasing order are as follows: W, Nb, Ni, Cr, Fe, Mg, K [67, 34]. From a thermodynamic point of view, alloying nickel with W and Nb may be beneficial since these are the two elements with a higher redox potential in molten chloride salts and are thus expected to be less susceptible to dissolution [68, 69]. Delpech et al. recently reviewed a wide range of materials under investigation for structural applications in nuclear systems with molten salts [70] and suggested alloying with Nb and the replacement of Mo with W, which showed stronger mechanical performance and corrosion resistance at high temperatures. A number of recent investigations [71, 72, 73] also concluded that alloying Ni with Nb would be beneficial for MSR applications because of niobium's good corrosion resistance. Prescott et al. and Ai et al. experimentally investigated W's corrosion resistance to Cl and reported negligible degradation in tungsten rich samples [74, 66], indicating alloying Ni with W does lead to improved corrosion resistance. Nb and W have been experimentally examined together, as well, where it was concluded that the presence of W and Nb enhanced the corrosion resistance of $\text{FeNi}_{25}\text{Cr}_{15}\text{W}_2\text{Nb}_2\text{V}_1$, especially at elevated temperatures [75]. Here, we employ density functional theory (DFT) to examine the surface corrosion performance of a representative system, $\text{Ni}_{70}\text{W}_{20}\text{Nb}_{10}$, in the presence of Cl to gain more insight into the suitability of Nb and W as alloying elements for MSR applications from a corrosion resistance point of view. Because the role of Cr in a Ni alloy has been thoroughly reviewed and explored [76, 70, 59, 77, 78] we omitted it from our representative alloy.

4.2 Computational Method

4.2.1 Bulk Structure

The bulk structure was generated using our implementation [38] of the multi-cell Monte Carlo solid-state phase prediction algorithm (see supplemental material for complete description of the MC algorithm) [1, 2]. The simulation was performed at $T = 800^{\circ}\text{C}$ and $P = 0$ bar, with the three simulation cells containing 32 atoms per cell in initial configurations of face-centered cubic (FCC), body-centered cubic (BCC), and BCC. Spin-polarized DFT calculations were performed using the Projector Augmented Wave (PAW) method as implemented by the Vienna ab initio Software Package (VASP) [3, 4]. The calculations were performed with a plane wave cutoff energy of 450 eV and a 3x3x3 Monkhorst-Pack [5] k-point mesh. DFT calculations performed on the simulation cells allowed for changes in the volume and atomic positions through the setting ISIF = 3. The electronic self-consistent calculation was converged to 1×10^{-6} eV and ionic relaxation steps were performed using the conjugate-gradient method (IBRION = 2) and continued until the total force on each atom dropped below a tolerance of 1×10^{-2} eV/Å. The generalized gradient approximation (GGA) was used for the exchange correlation functionals as parameterized by Perdew-Burke and Ernzerof (PBE) [21]. The PAW pseudopotentials [4] were used with the valence electron configurations $3\text{d}^84\text{s}^2$, $4\text{p}^65\text{s}^14\text{d}^4$, and $6\text{s}^25\text{d}^4$ for Ni, Nb, and W, respectively.

4.2.2 Surface Study

Once $(\text{MC})^2$ reached equilibrium, the bulk configuration with the highest molar fraction value was extracted and surface slabs were generated from it. In our case, this corresponded to the 2nd simulation cell, a body-centered tetragonal (BCT) crystal structure with a molar fraction value of 97%. Surface slabs along the (100), (110), and

(111) directions were generated using our surface slab tool [79]. The bulk structure, as seen in VESTA [80], and surface cuts are shown in Figure 23. Surface terminations were chosen such that each slab contained all members of the alloy to maximize insight on how the chlorine interacted with different members of the alloy. The surface slab with the lowest surface energy was chosen for additional study; for this work it was the (110) slab. The surface slabs consisted of 4 layers, 2 to represent the surface, and 2 to represent the bulk, and a vacuum layer of 20 Å along the \hat{c} direction to prohibit interaction between image slabs. Selective dynamics was used to freeze the bulk layers while the surface layers and Cl-adsorbate(s) were free to move in the \hat{a} , \hat{b} , and \hat{c} directions.

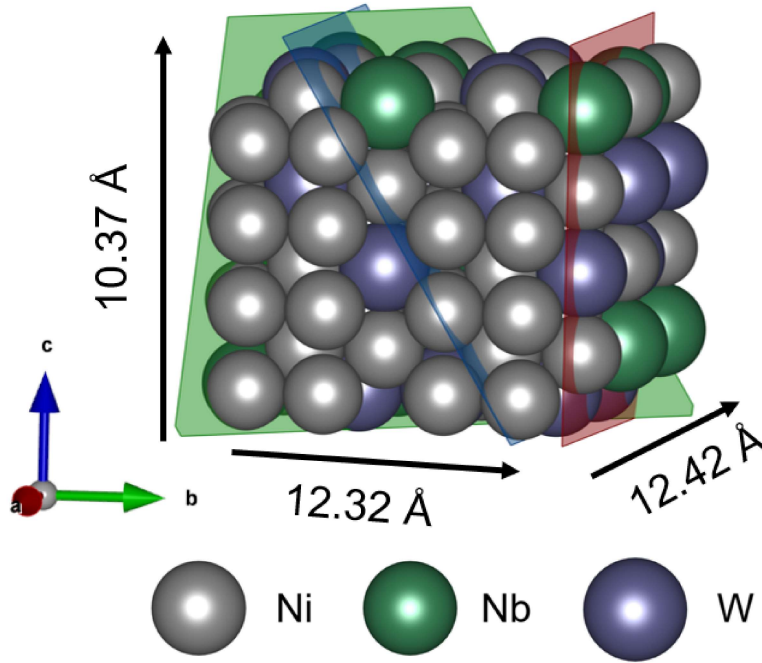


Figure 23. The body-centered tetragonal bulk structure multiplied into a larger supercell for surface cuts. The (010), (011), and (111) surface planes are shown in red, blue, and green, respectively.

Spin-polarized DFT calculations were executed with a plane wave cut-off energy of 600 eV and a 4x4x1 Gamma-point-centered Monkhorst-Pack k-point grid [5]. The

electronic energy was converged with respect to the k-point grid and energy cut-off to within 1 meV. Through propagation of error in the electronic energies, surface energies were reported with confidence up to 0.1 meV/Å². Electronic relaxation was converged to 1x10⁻⁶ eV and ionic relaxation steps were continued until a force tolerance criterion of 1x10⁻² eV/Å was satisfied. The PAW pseudopotentials had the same valence electron configurations as stated in the previous subsection, with the addition of an electron valence configuration of 3p⁵3s² for chlorine. The surface energy per unit area is given by,

$$E_{surf} = \frac{1}{2A} (E_{slab} - NE_{bulk}), \quad (33)$$

where A is the area of the surface slab, in units Å², E_{slab} is the total energy of the the surface slab, in units of eV, N is the number of atoms present in the surface slab, and E_{bulk} is the energy per atom of the bulk structure from which the surface slab was cut, in units of eV/atom.

Spin-polarized adsorption calculations were executed using an energy cut-off of 600 eV, an electronic relaxation convergence setting of 1x10⁻⁶ eV, and force tolerance criteria of 1x10⁻² eV/Å. Electronic energies were converged with respect to the k-point grid and plane wave cut-off energy to within 1 meV. Chlorine was initially adsorbed in the molecular form of Cl₂; however, it preferred to adsorb in the dissociated form. Similar ab initio investigations of Cl adsorption to metal surfaces observed the same preference [81, 82, 83]. Therefore, Cl was adsorbed in the dissociated form. Eight adsorption events were carried out in regions of varying Ni, Nb, and W content. Figure 24 (a) shows a top-down view of the surface model with the initial placement of the Cl adsorbates marked. Each Cl adsorbate was introduced 3.2 Å above a hollow site. Figure 24 (b) is a full view of the slab model with the dimensions labeled and the vacuum region shown.

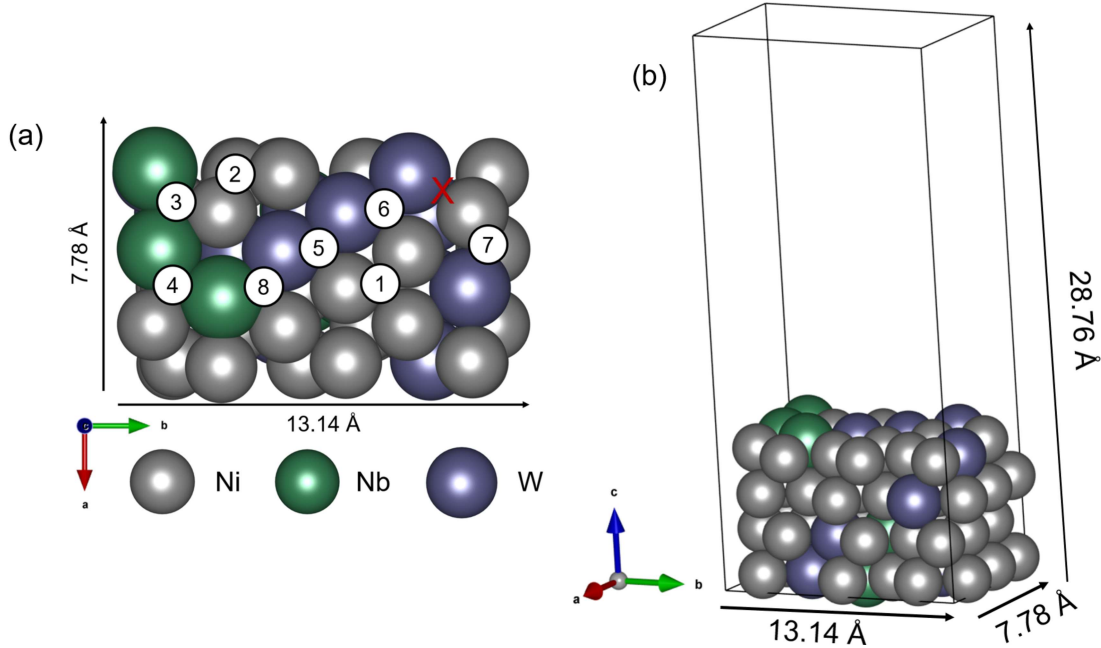


Figure 24. The (110) surface slab with the eight hollow adsorption sites labeled. Because many of the chlorine atoms settled to a bridge adsorption site, one has been marked with a red X in the upper right corner. (b) The surface slab model with the cell bounds displayed.

The adsorption energy is given by [76],

$$E_{ads} = -\frac{1}{n} \left(E_{slab}^{Cl(n)} - E_{slab} - \frac{n}{2} E_{Cl_2} \right) \quad (34)$$

where $E_{slab}^{Cl(n)}$ is the total electronic energy of the slab with adsorbed Cl, E_{slab} is the total electronic energy of the clean slab, n is the number of Cl atoms present, E_{Cl_2} is the energy of the gas phase Cl_2 molecule. The electronic energy of Cl_2 was calculated by relaxing the positions of two Cl atoms in a box of dimensions (12, 12, 12) Å until the force on each atom was below 1×10^{-2} eV/Å. The calculated molecular electronic energy was -3.36 eV. To measure the accuracy of this value we calculated the Cl_2 binding energy, $BE = E_{Cl_2} - 2E_{Cl}$, and report it to be 2.84 eV which is overestimated when compared to the known value of 2.51 eV [84]. This overestimation is attributed to the use of the PBE exchange-correlation functional [85, 86]. As defined in equation

34, a more positive adsorption energy denotes a more favorable reaction.

To study the mechanisms of attack, Cl was systematically introduced around a Ni, Nb, and W atom up to five Cl atoms. Figure 25 shows the clean surface slab with the attacked Ni, Nb, and W atoms encircled in black. The green and red rings show the approximate area that was scanned to introduce each atomic Cl adsorbate. The favored adsorption sites within the green ring were occupied first, followed by favored adsorption sites between the green and red ring. The Cl adsorbates were free to move in all three directions. The adsorption energies were calculated using equation 34 for each attack at each Cl coverage, from 1/15 monolayer (ML) up to 5/15 ML. We considered 1 ML to represent a complete occupation of the 15 available hollow sites on the surface layer. The desorption energy for each attack from 0 ML up to 5/15 ML was calculated using equation 35. To accurately report the favorable desorbate, we considered all possible desorbates with each new Cl adsorbate. For example, with the NiCl_5 event, we consider the desorption of, 1) Ni, 2) NiCl , 3) NiCl_2 , 4) NiCl_3 , 5) NiCl_4 , and 6) NiCl_5 . Additionally, all permutations of molecular Cl and metal-chloride desorbates were trialed to find the combination that was energetically favored to desorb.

$$E_{des} = (E_X + E_{slab-X}) - E_{slab+X} \quad (35)$$

In equation 35, E_X is the electronic energy of the X molecule in vacuum, i.e. Cl_2 , NbCl , WCl , NiCl , etc., E_{slab-X} is the electronic energy of the desorbed surface slab, and E_{slab+X} is the electronic energy of the slab with the X compound adsorbed. E_X energies were calculated by relaxing the X compound in a box of dimensions (15, 15, 15) Å.

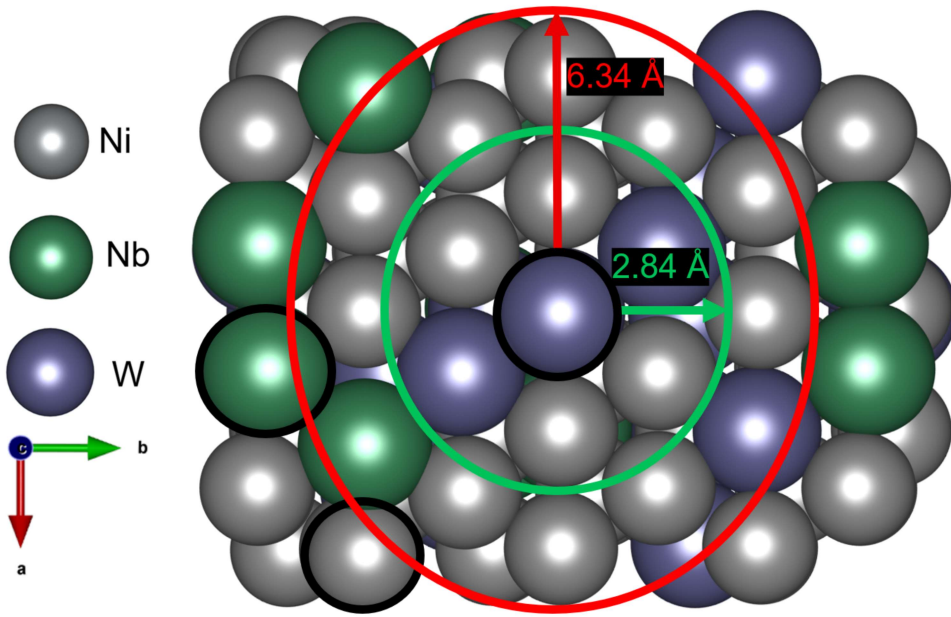


Figure 25. The clean surface slab with the chlorine-attacked niobium, nickel, and tungsten atoms encircled in black. For this example, the green and red ring indicate the approximate areas that were scanned to introduce attacking atomic chlorine around tungsten. The same procedure was followed for the nickel and niobium attacks.

To quantify the impact Cl adsorption has on the alloy's resistance to radiation damage, the vacancy formation energy for creating a Ni, Nb, or W vacancy at varying Cl coverage was calculated using equation 36 from 0 ML to 5/15 ML. For each attack, one Nb, Ni, or W vacancy was introduced per Cl coverage. The Nb, Ni, and W atom that was deleted is encircled with a black ring in Figure 25.

$$E_{vac} = \frac{1}{n}(E_{slab} - E_{slab+vac} - nE_M^{bulk}) \quad (36)$$

As listed in equation 36, n is the number of vacancies, which was 1 in this study, E_{slab} is the electronic energy of the clean or chlorinated slab without the vacancy, $E_{slab+vac}$ is the electronic energy of the clean or chlorinated slab with the vacancy, and E_M^{bulk} is the electronic energy per atom of the bulk metal system (Ni, Nb, or W). As it is defined, a negative E_{vac} value represents an endothermic reaction; the more negative

the value, the more energy required to produce the metal vacancy.

The Gibbs free energy of formation per atom was calculated for the Nb and W attack configurations at 1/15, 2/15, and 3/15 ML using equation 37. We did not go beyond 3/15 ML because events beyond this would not be studying Cl adsorption *to a Nb or W atom*. The reason we did not include the Ni attack configurations is because only one Cl atom actually adsorbed to the targeted Ni. The results would not accurately describe the thermodynamics of adsorption *to a nickel atom*.

$$\Delta G = \left(E_{slab}^{Cl(n)} + F_{vib} - E_{slab} - n\mu_{Cl}(T, P) - TS_{mix} \right) / (N + n) \quad (37)$$

In equation 37, $E_{slab}^{Cl(n)}$ is the total electronic energy of the oxidized slab, E_{slab} is the total electronic energy of the clean slab, N is the number of metal atoms, and n is the number of Cl atoms present. F_{vib} is the Helmholtz vibrational energy which was considered within in the harmonic approximation for the adsorbed Cl atoms only. The phonon normal mode frequencies were calculated using the finite-difference method as implemented by VASP (IBRION = 5) with Γ -point sampling only. The term μ_{Cl} represents the chemical potential of chlorine and is expressed as,

$$\mu_{Cl}(T, P_{Cl}) = \frac{1}{2}E_{Cl_2} + \Delta\mu_{Cl}(T, P_{Cl}). \quad (38)$$

The first term in equation 38 is the energy of the gas phase Cl_2 molecule. The second term, $\Delta\mu_{Cl}$ is a correction term which is treated as a parameter and is expressed as,

$$\Delta\mu_{Cl}(T, P_{Cl}) = \frac{1}{2} \left(\mu_{Cl_2}^0 + k_B T \ln \left(\frac{P_{Cl}}{P^0} \right) \right). \quad (39)$$

The term $\mu_{Cl_2}^0$ in equation 39 is the difference of the chemical potential of Cl_2 at $T = 0$ K and $T > 0$ K under $P = 1$ atm and can be calculated at various temperatures,

while holding the pressure constant, using the value reported for a given temperature in the National Institute of Standards and Technology (NIST) Joint Army-Navy-Air Force (JANAF) Thermochemical tables for Cl₂ [87, 41, 42]. The entropy of mixing, S_{mix} , in equation 37 is defined in equation 40 and is a constant value in this case, because the atomic concentrations of each species, x_i , are unchanged.

$$S_{mix} = -k_B \sum_{i=1}^3 x_i \ln(x_i) \quad (40)$$

For this study, P⁰ was set to 1 bar and the system was analyzed in the temperature range of 430°C to 930°C and pressure range of 10⁻⁴⁰ bar to 10⁻⁵ bar. For each set of (T,P) the coverage with the lowest Gibbs free energy was identified and a stability plot was produced. The temperature bin width for both stability plots was 100°C which is restricted to that of the JANAF tables.

4.3 Results & Discussion

(MC)² predicted a BCT structure with lattice constants a, b, c = 6.21, 6.16, 3.46 Å and lattice angles $\alpha, \beta, \gamma = 89.8, 90.3, 93.3$ degrees. The molar fraction of this phase was 97% and the atomic composition was Ni₇₂W₁₉Nb₉ (i.e., Ni₅₀W₄₀Nb₁₀ by weight percent) at T = 800°C and P = 0 bar. To examine the skewing of the crystal structure, the (MC)² simulation cell was transferred into a perfect BCC structure and relaxed. From this, it was determined that the skewing of the crystal structure was an artifact of the electronic relaxation and varying sizes of the atomic species. To correct for this, the lattice angles were set to 90° before surface cuts were generated. A comparison to the Ni-Nb and Ni-W phase diagrams at 800°C near 20 atom % Nb and W found that the Ni-Nb alloy exhibits largely an orthorhombic phase, Ni₃Nb [88, 89], and the Ni-W alloy exhibits a complete BCT phase, Ni₄W [90]. While a

ternary phase diagram was not found, the $(MC)^2$ results match well with the Ni_4W BCT structure, whose lattice constants are $a = b = 5.73 \text{ \AA}$ and $c = 3.55 \text{ \AA}$, when we account for an increase in the lattice size as a result of the varying sizes of Ni, Nb, and W as they occupy different lattice sites. The final results of the $(MC)^2$ algorithm are reported in Figure 26, where (a) is the final atom % of each simulation cell and (b) is the final molar fraction of each simulation cell. The uncertainty in the reported atom % values was 3.125%. The uncertainty in the reported molar fraction values were 0.276%, 0.289%, and 0.563% for three simulation cells, respectively.

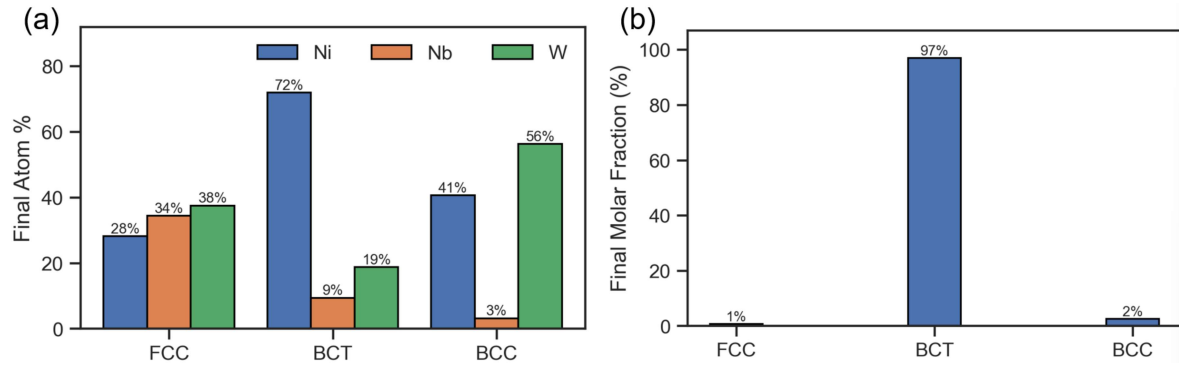


Figure 26. (a) The final atom percent of the three simulation cells which are labeled based on the final crystal structure they exhibited. (b) The Final Molar Fraction of the simulation cells. For reference, the initial molar fractions of each cell was 33.3% for each cell.

The BCT structure had a Bulk Modulus of (183, 187) GPa, a Shear Modulus of (96, 273) GPa, and a Poisson’s Ratio of 0.125. Figure 27 (a) shows the projected density of states (PDOS) for the bulk structure. Figure 27 (b) is a histogram of each species’ distribution of states over the s-, p-, and d-orbitals. From Figure 27, we see that Nb had a high number of d-orbital states available near the Fermi level and this led to a strong interaction between Cl and Nb on the (110) surface.

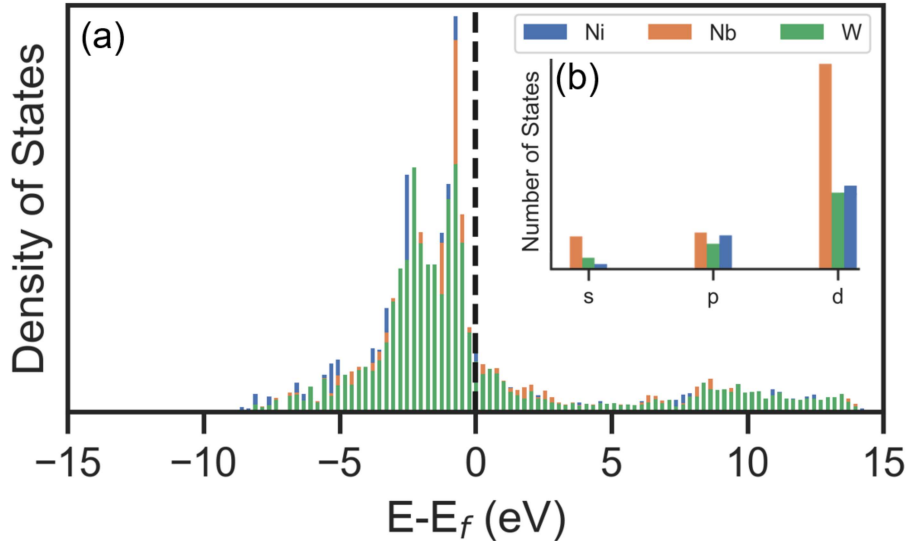


Figure 27. (a) The projected density of states for the nickel (Ni), niobium (Nb), tungsten (W) alloy. (b) State distribution over the s-, p-, and d-orbitals.

The surface energy values for the (100), (110), and (111) surfaces were 187.6, 148.6, and 154.7 meV/ \AA^2 , respectively. The adsorption study was carried out on the energetically favored (110) surface slab. Figure 28 shows the relaxed (110) surface of the 8 adsorption events examined in this study. Table 6 lists the adsorption energies at 1/15 ML, as well as, the metal species present at the adsorption site. Two metals listed indicates the adsorption event ended at a bridge position while three metals indicates the final position was a hollow site.

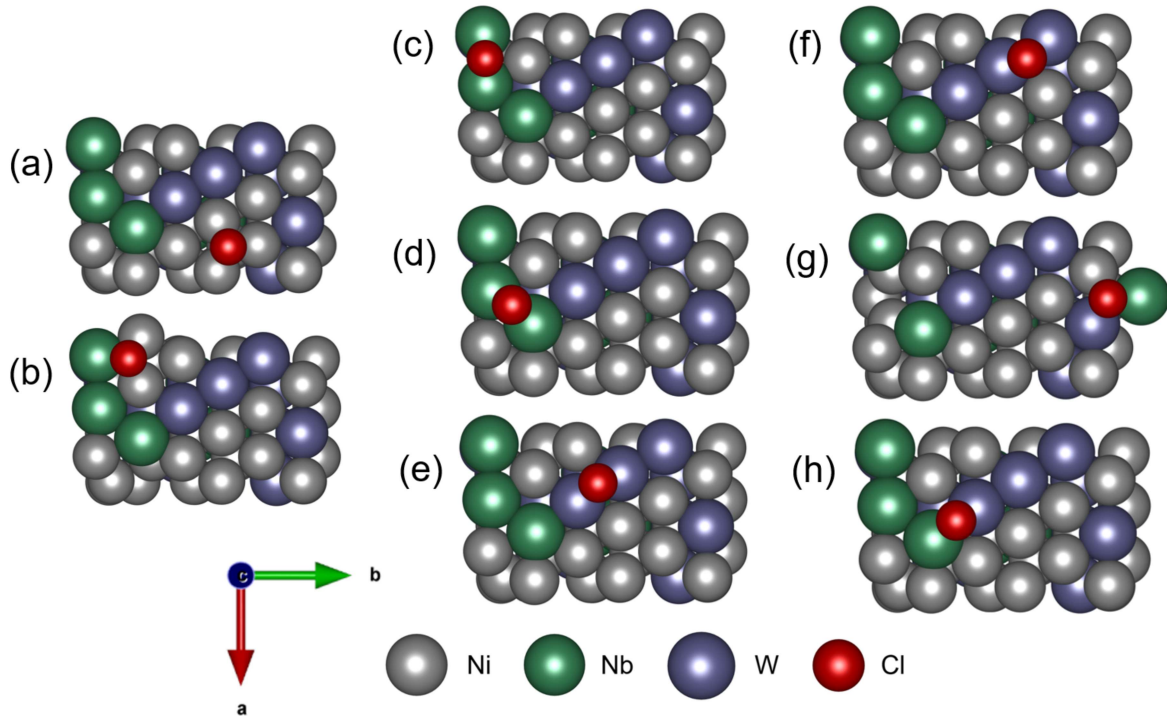


Figure 28. The final configurations of the eight chlorine adsorption events.

Cl preferred the region rich in Nb, where the highest adsorption energies were reported. Cl relaxed to sites with Nb in Figure 28 event (b), (c), and (d). When Nb_2 or W_2 was present at the adsorption site the Cl settled at the bridge adsorption site. The lowest adsorption energy was observed at a pure Ni hollow site. The average adsorption energy on this surface was 2.65 eV.

Table 6. The adsorption energy values at 1/15 ML for the events displayed in Figure 28, listed in the same order. Three metals listed indicates a hollow site while two atoms represents a bridge site. A more positive value indicates a more favorable reaction.

Ads. Energy (eV)	Nearest Metallic Neighbors
1.937	Ni ₃
2.459	Ni ₂ , Nb
3.015	Nb ₂
3.068	Nb ₂
2.628	W ₂
2.513	W ₂
2.669	Ni, Nb, W
2.965	Nb, W

The progression of the Ni, Nb, and W attacks are shown in Figure 30 (a), (b), and (c), respectively. For the Ni attack, Figure 30 (a), the first and second Cl relaxed upwards ($-\hat{a}$ direction) and settled into a Nb₂ and NbW bridge site, respectively. The third Cl adsorbed to a Ni₂Nb hollow site. The fourth and fifth Cl adsorbed to a Ni₃ hollow site and NiW bridge site, respectively. Considering the 1/15 ML and 2/15 ML adsorption events of the Ni attack, this marks the fourth and fifth time we have reported relaxation of Cl to Nb sites. It is clear that Nb acted as a trapping sink on this surface. For the Nb attack, Figure 30 (b), the first and second Cl adsorbed to Nb₂ bridge sites and the third Cl adsorbed to a NbW bridge site. The fourth and fifth Cl adsorbed atop of W atom and to a W₂ bridge site, respectively. For the W attack, Figure 30 (c), the first and second Cl adsorbed to a W₂ bridge site and the third Cl adsorbed to a Ni₂ bridge site. The fourth Cl adsorbed to a Ni₂ bridge site and the fifth Cl relaxed atop a Nb in response to repulsion from the 4 Cl atoms previously adsorbed to the surface. The metal-chloride bond lengths are reported in

Figure 29 as a function of Cl coverage. Nb-Cl bonds stayed fairly constant as coverage increased while Ni-Cl bonds showed the largest variation in length as Cl adsorbed to the surface. The average movement along the \hat{c} direction of the metal species which were bound to one or more Cl atoms was calculated across all three attack events. The average perpendicular movement of Ni, Nb, and W was 0.03262 Å, 0.2595 Å, and 0.1415 Å, respectively. Five out of the eleven instances of Ni-Cl bonds forming resulted in Ni moving inwards ($-\hat{c}$ direction) while Nb and W only moved outwards ($+\hat{c}$ direction). Overall, Nb showed the strongest response to the adsorbed Cl with Ni and W showing comparable response in magnitude but not direction. The average distance between the first and second surface layer at 5/15 ML showed an increase, relative to the initial separation at 0 ML, by 0.01078 Å, 0.02531 Å, and 0.01780 Å for the Ni, Nb, and W attacks, respectively.

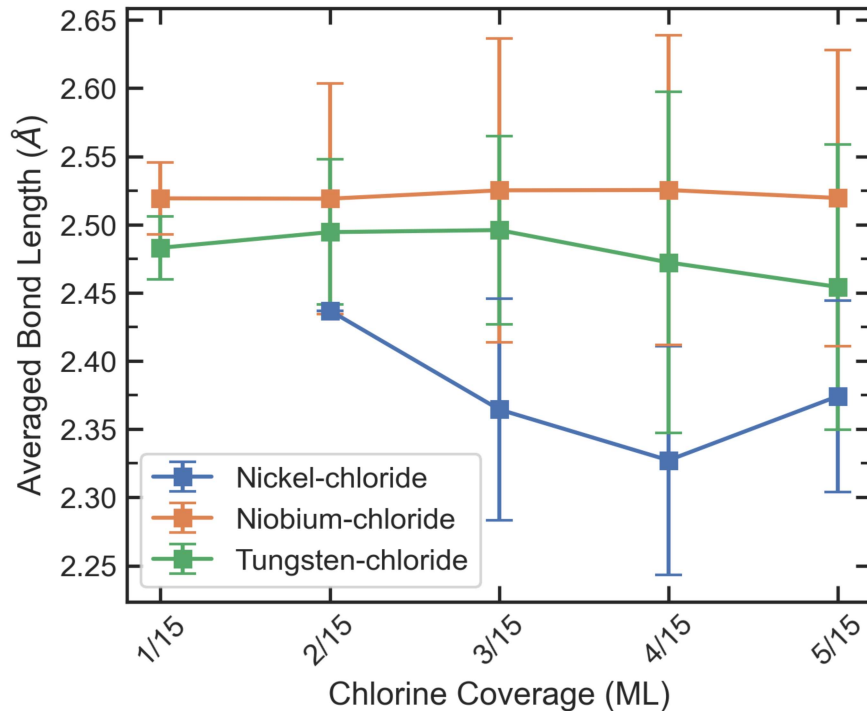


Figure 29. The averaged bond lengths for nickel-, niobium-, and tungsten-chloride bonds. The average included metal-chloride bonds that formed across all three attack events.

The adsorption energies for the events depicted in Figure 30 (a), (b), and (c) are shown in Figure 30 (d), where a more positive value indicates a more thermodynamically favorable process. A green and red line mark the “boundaries” of the green and red search rings depicted in Figure 25. Several observations can be gleaned from examining the adsorption energies. First, adsorption to Nb was favored over W or Ni at 1/15 ML, supporting our earlier result from the eight adsorption events, but also at 2/15 and 3/15 ML. Please note, the first two adsorption events of the Ni attack (blue square markers in Figure 30 (d)) were to a Nb₂ site and NbW site, respectively. Second, that Cl aggregation in the Nb-rich region was favored over Cl adsorption to “clean” W or Ni up to 3/15 ML. If we consider the Cl adsorption events within the green search circle, 1/15 ML, 2/15 ML, and 3/15 ML data points in Figure 30 (d), all three metal attacks exhibited a decrease in adsorption energy; however, Cl adsorption to W resulted in the quickest descent, with a ΔE_{ads} of about 1 eV, while Cl adsorption to Nb slowly decreased, with a ΔE_{ads} of about 0.25 eV. This indicates that aggregation of Cl around W or Ni is less thermodynamically favorable than Cl aggregation around Nb. This is in good agreement with our observation that Nb acts as a trapping sink within this surface. The large increase in the adsorption energy of the 4/15 ML Nb attack event, Figure 25 (d) fourth orange event, was the result of Cl relaxing atop a nearby W atom in response to Cl-Cl repulsion from the already adsorbed first and third Cl atoms.

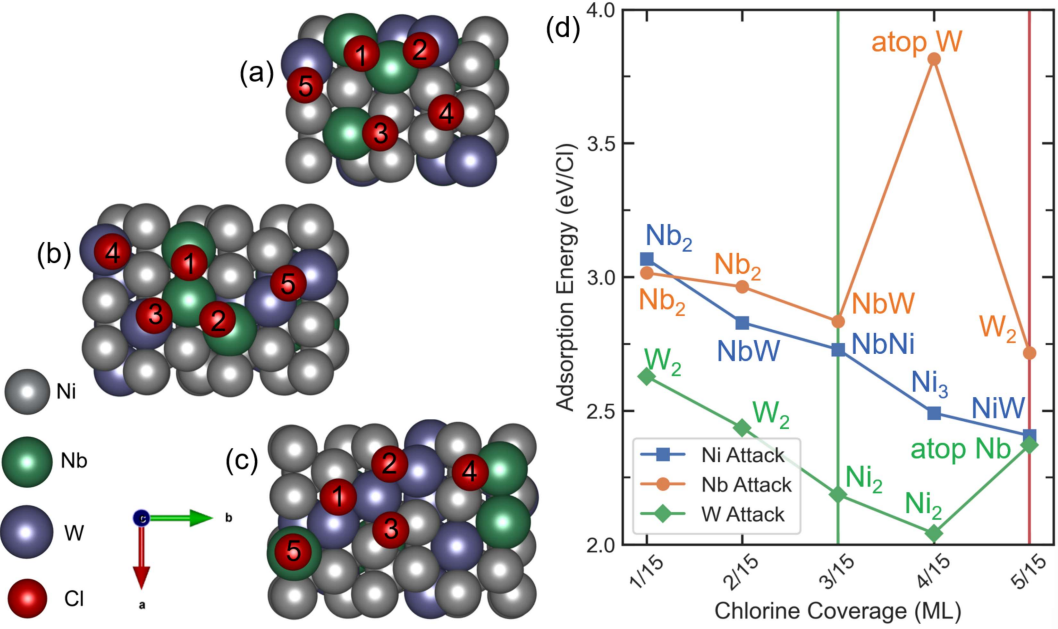


Figure 30. The progression of the (a) nickel, (b) niobium, and (c) tungsten chlorine attacks up to a chlorine coverage of 5/15 ML. (d) The adsorption energies for the events depicted in (a) blue, (b) orange, and (c) green with the nearest metallic neighbors labeled. The green and red vertical lines indicate sites within the boundaries of the search rings shown in Figure 25.

To further study the corrosivity of the surface in the presence of chloride salts, desorption energies for the different Cl-containing species are shown in Figure 31 (a), (b), and (c) were calculated and are reported in Figure 31, where a lower value indicates a more energetically favored process. First, regardless of which metal was attacked, the favored desorbate was atomic chlorine, Cl. This fact is clear in Figure 31 (a), (b), and (c) where Cl (black line with triangles) is the lowest curve on the plot. The values reported in Figure 31 correspond to the atom or molecule which generated the lowest desorption energy. As Cl content increased so did the number of permutations that we needed to scan for potential desorbates. The Cl and Cl_2 desorption energies decreased with increased Cl coverage, this indicates that additional Cl adsorbed nearby encouraged atomic and molecular Cl desorption. Of the three metals, Cl and Cl_2 are predicted to desorb from a Ni or W atom more readily than from a Nb atom, as the desorption energies for Cl and Cl_2 were lowest for the Ni and W attacks. Addition-

ally, the 5/15 ML W-attack event, Figure 31 (c), was Cl adsorbing atop a Nb atom which resulted in an increase of desorption energies, ΔE_{des} between 0.5 and 1 eV, for any Cl or tungsten-chloride species. This suggests that the probability of Cl removal is reduced once Nb-Cl bonds form. It may also indicate that forming Nb-Cl bonds protects nearby metal atoms from Cl-assisted dissolution. These observations further support the thermodynamic likelihood that Cl will aggregate in Nb-rich regions. In this study, Ni, Nb, and W resisted Cl-facilitated dissolution from the surface slab up to 5/15 ML, as all metal-chloride curves in Figure 31 remained above the Cl curve. Nevertheless, the values and trends of the different metal-chloride desorption energies does provide useful insights. For Ni, its most susceptible dissolution pathway was in the form of NiCl_2 followed by NiCl . Nickel-chloride formed with three or more Cl, $\text{NiCl}_{\geq 3}$, appeared to be highly resistant to Cl-facilitated dissolution; this sets Ni apart from Nb and W which were more susceptible as local Cl content increased. For Nb, its most susceptible dissolution pathway was in the form of NbCl_4 followed by NbCl_3 . We also observed Nb had the strongest outward response once Nb-Cl bonds were formed. For W, its most susceptible dissolution pathway was WCl_4 followed by WCl_2 . Comparing the lowest metal-chloride data point at 5/15 ML between all three metals shows that NiCl_2 , E_{des} about 4 eV, was the most susceptible to Cl-facilitated dissolution, followed by NbCl_4 , E_{des} about 4.5 eV, and WCl_4 , E_{des} about 5.25 eV, thanks to a nearby Nb-Cl bond. Despite the fact that no metallic dissolution was observed, it is expected that metal-chloride desorption would become more favorable as Cl coverage continued to increase.

A similar first principles study was conducted on the adsorption of fluorine to the Ni(111) surface doped with Cr [76], which has been experimentally confirmed to undergo intense dissolution in the presence of a fluoride and chloride molten salt at MSR temperatures [59, 77, 78]. The authors reported CrF adsorption energies be-

tween 3 and 3.5 eV/adsorbate and favorable dissolution of Cr in the form of CrF_2 and CrF_3 whose desorption energies were about 3 and 2 eV, respectively. Pavlova et al. executed a DFT study on the adsorption and desorption of Cl onto the Cu(111) surface [82]. The authors reported Cl adsorption was favorable on the Cu(111) surface, with adsorption energies around 2 eV/adsorbate. The favored desorbate was CuCl , with an average desorption energy of 2.68 eV. Nickel's superior corrosion resistance is well-known and has been experimentally measured [64, 65]. Ai et al. experimentally demonstrated the superior corrosion resistance of W in the alloy $\text{NiW}_{26}\text{Cr}_6$ where they report only slight depletion in the region rich with W in the presence of FLiNaK molten salt [66]. Prescott et al. experimentally examined several different metals exposed to an argon-25%H₂-10%HCl-5%CO-1%CO₂ gas at 900 °C and concluded Mo and W showed the strongest resistance against Cl-assisted corrosion effects [74]. Smith and Eisinger experimentally explored the corrosion resistance of Ni-Cr-Mo-W with the addition of Nb (up to 4 wt.%) in the presence of different aqueous solutions at $T > 650^\circ\text{C}$ and reported excellent performance against HCl at most concentrations and temperatures; but very poor resistance to HF which is important to note for MSR designs which utilize F-containing molten salts [72]. Andrianingtyas et al. doped austenitic stainless steel with Nb and W and reported that samples with Nb and W present displayed the highest resistance to pitting corrosion, which increased at elevated temperatures [75]. Combining the experimental observations on W and Nb corrosion resistance with the magnitude of theoretical adsorption and desorption energies reported by Yin et al. and Pavlova et al., our findings support the experimental conclusions that Nb and W exhibit strong resistance to Cl. Furthermore, from our reported adsorption energies for Ni compared against Nb and W, we found that Cl has a thermodynamic preference to adsorb to Nb (followed by W) over Ni. Couple this observation with the reported desorption energies, which showed W (followed by

Nb) possessed a stronger resistance to Cl-assisted dissolution than Ni, it is suggested that Nb and W enhanced the corrosion resistance of Ni. From a thermodynamic point of view, it appeared that Nb and W protected Ni from Cl adsorption by creating more favorable adsorption regions (especially true of Nb) which are more resistant to metal-chloride dissolution (up to 5/15 ML). These observations on Nb and W protection are consistent with experimental studies mentioned throughout this paragraph as well as with studies on Ni-containing ferritic stainless steels which reported increasing Nb [71] and W [91] content reduced the severity of chlorine facilitated corrosive pitting in the alloy samples.

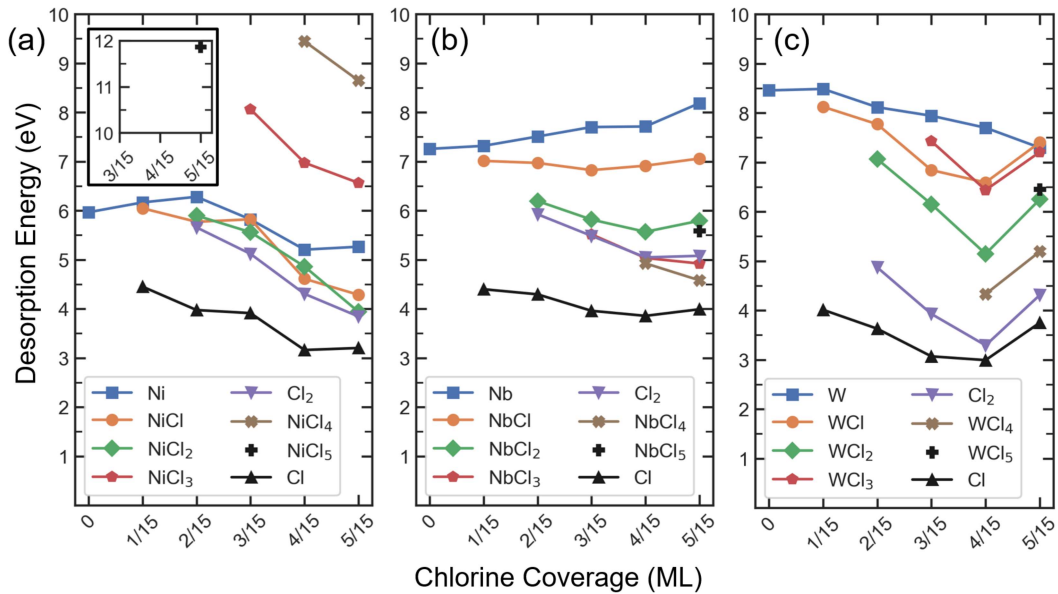


Figure 31. Desorption energies for metal, M, atoms and metal-chloride, MCl_X , molecules, where $M =$ (a) Ni, (b) Nb, (c) W and $X = 1, 2, 3, 4, 5$. Atomic chlorine, Cl, and molecular chlorine, Cl_2 , desorption energies are listed, as well. The (a) inset shows the location of the $NiCl_5$ data point.

Because radiation damage should be anticipated in an MSR environment, we examined the relationship between Cl coverage and the formation of surface defects in the local area. The vacancy formation energy for a Ni, Nb, and W vacancy was calculated from 0 ML to 5/15 ML using the configurations generated by the Cl attacks and are reported in Figure 32. For a Ni vacancy, the formation energy initially de-

creased, as Nb-Cl bonds formed, but then increased as more Cl adsorbed locally. For Nb, the vacancy formation energy steadily decreased as Cl adsorbed nearby. For W, the vacancy formation energy steadily increased as Cl adsorbed nearby. Our findings suggest that Nb is bolstered against ejection from the surface slab due to an incident radiation particle while Ni and W are more susceptible to radiation damage as local Cl content increases. It could be that Nb plays a dual role in MSR applications. In addition to improving the nickel alloy's radiation resistance, it may also harden the alloy against radiation damage. On the contrary, while W possessed superior resistance against Cl-dissolution, it may reduce the alloy's resistance to ambient radiation.

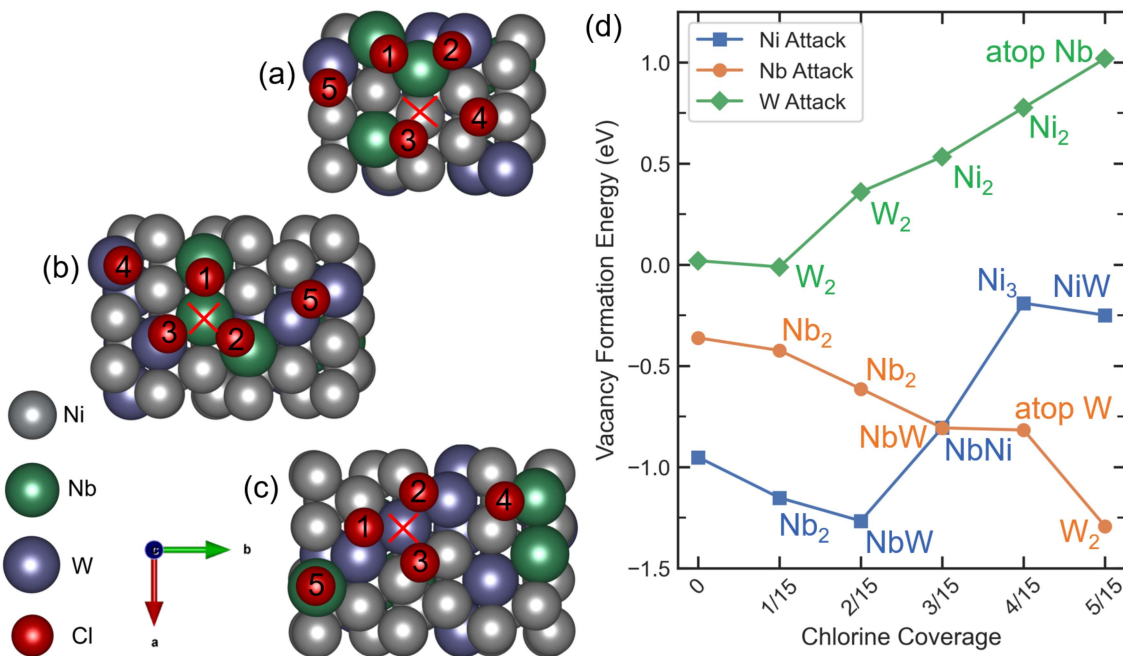


Figure 32. The progression of the (a) nickel, (b) niobium, and (c) tungsten chlorine attacks up to a chlorine coverage of 5/15 ML. The vacancies are marked with a red X. (d) The vacancy formation energies for a nickel (blue), niobium (orange), and tungsten (green) as local chlorine content was increased. The nearest metallic neighbors to the adsorbed chlorine are labeled.

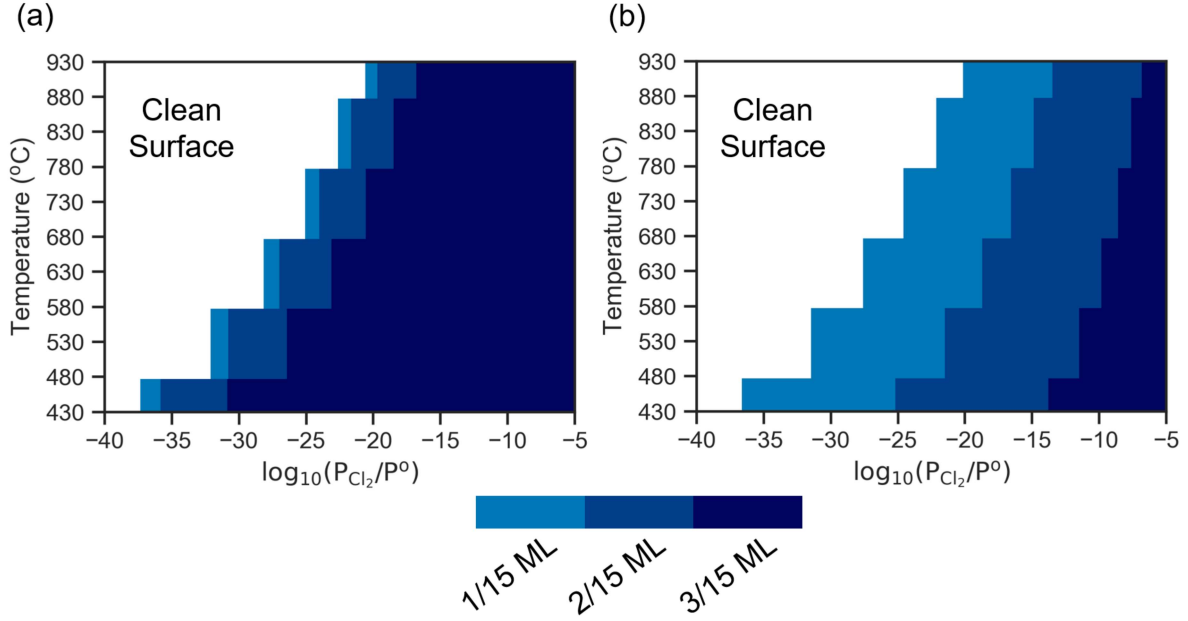


Figure 33. (a) Surface stability plot examining chlorine adsorption to the region rich with niobium. (b) Surface stability plot examining chlorine adsorption to the region rich with tungsten.

Since chlorine adsorption is the first step towards activating the dissolution of metallic atoms, it was important to study the thermodynamics of chlorine adsorption. Examining the surface coverage in the region rich with Nb and W at different (T,P) values resulted in two stability plots, shown in Figure 33. Plot (a) is in the region rich with Nb, where 3/15 ML Cl coverage is achieved far more quickly than in the region rich in W, plot (b). Near 800°C, the W-rich area did not see 3/15 ML until around 10^{-7} bar, while the Nb-rich region of the surface reached 3/15 ML by 10^{-17} bar. Therefore, the presence of Nb increased the thermodynamic stability of the chlorinated surface. This result is in good agreement with our results on Nb from studying the adsorption energies in Figure 30 (d) and could further explain why chlorine and metal-chlorine desorption were thermodynamically less likely to occur as Nb-Cl bonds formed.

The findings of this work are a first step towards uncovering a deeper understanding on the behavior of structural materials in a molten salt environment. The

results reported here are in good agreement with the preliminary experimental findings, however this study was conducted with limitations. The surface analysis was restricted to a single (110) surface, so results should not be generalized. A more thorough investigation would include additional (110) structures and examine surface models from the {100} and {111} family. Anharmonic vibrational corrections to the metal atoms and Cl adsorbates were not applied and could play an important role under certain conditions. Additionally, vibrational corrections were not considered for the surface slab or desorbates during the desorption calculations. At elevated temperatures, desorption of the species considered within this work would likely be more thermodynamically favorable. The simulation cell executed in (MC)² was only a 4x2x2 supercell, restricting the size of the surface structures studied here. A larger surface slab is less susceptible to image interactions and would generate a larger sample of adsorption and desorption events to draw conclusions from. Exploring higher Cl coverage would allow for the creation of more metal-chloride systems which would provide further insight on the system's corrosion resistance. Studying more vacancy + chlorine combinations would generate a better understanding on the coupling between corrosion and radiation damage. During the thermodynamic study we scanned the (T,P) domain but did not account for phase transitions of the bulk material. The most accurate results of the stability plots are reported around 800°C.

4.4 Conclusion

The surface corrosion resistance of Ni₇₀W₂₀Nb₁₀ was examined through the employment of density functional theory, a multi-cell Monte Carlo method, and thermodynamic modeling. Incoming chlorine showed a thermodynamic preference to Nb, likely caused by the high number of unfilled d-orbital states available among the niobium atoms. The preferred adsorbed position of chlorine was at the bridge site

when Nb_2 or W_2 was present and the hollow site when only Ni or Ni, Nb, and W were present. The local resistance to corrosion was examined for nickel, niobium, and tungsten. Our findings suggested that niobium and tungsten enhanced the corrosion resistance of nickel by creating regions which were thermodynamically preferred by the incoming chlorine and less susceptible to chlorine-facilitated dissolution from the surface model up to 5/15 ML. Nickel, niobium, and tungsten resisted chlorine-induced dissolution from the surface model up to 5/15 ML, indicating that all members of this alloy possessed superior resistance to localized surface degradation such as corrosive pitting. The strong resistance against chlorine facilitated degradation exhibited by this alloy was in good agreement with experimental reports on nickel's corrosion resistance and the improved corrosion resistance of alloys containing either niobium, tungsten, or both species in alloy samples. To quantify each species resistance to radiation damage, and chlorine's impact on that resistance, the nickel, niobium, and tungsten vacancy formation energies were calculated as local chlorine coverage increased. By doing so, we were simulating defects that would arise in the surface slab as a result of a collision cascade initiated by a primary knock-on atom (PKA). From this, it was determined that nickel and tungsten were more susceptible to radiation damaging effects as chlorine adsorbed nearby while niobium's radiation resistance was enhanced. Using thermodynamic modeling, we found that the stability of the chlorinated surface slab increased with the presence of Nb. This result is in good agreement with our findings on chlorine adsorption to niobium which showed that niobium acted as a trapping sink on this surface slab. Overall, our results indicated that the (110) surface of $\text{Ni}_{70}\text{W}_{20}\text{Nb}_{10}$ possessed superior resistance to Cl-induced surface degradation. Additional surface studies need to be conducted before any generalizations can be made on the corrosion resistance of $\text{Ni}_{70}\text{W}_{20}\text{Nb}_{10}$.

V. Conclusion

A multi-cell Monte Carlo algorithm was implemented based on a previously developed method. To demonstrate one of the many ways the algorithm could be used, two studies were carried out on the material degradation of an alloy system in an extreme environment. The first project was a computational investigation into the oxidation resistance of a candidate high-entropy alloy, $\text{Al}_{10}\text{Nb}_{15}\text{Ta}_5\text{Ti}_{30}\text{Zr}_{40}$, using $(\text{MC})^2$ to generate the solid-phase of the material at 1000 °C, cutting the thermodynamically stable surface from that phase, and attacking that surface with oxygen. Some of the main conclusions from that work included 1) the observation that the thermodynamic stability of the oxidized surface increased as oxygen adsorbed, 2) diffusion of oxygen into the bulk was likely to occur in regions rich with Zr at low oxygen coverage, and 3) that diffusion was protected against with the addition of Ti and Al. The second project investigated the corrosion resistance of a representative nickel-based alloy, $\text{Ni}_{70}\text{W}_{20}\text{Nb}_{10}$, in contact with chlorine. Some of the key results from that work included findings that supported the experimentally observed superior resistance to chlorine corrosion displayed by each metal constituent and the impact that chlorine plays on the local radiation resistance of the alloy surface. Both studies were executed to demonstrate a methodology to theoretically probe the resistance of candidate alloy systems against material degradation caused by their operational environments. Oxidation-based degradation was explored as it is a top contributor to material degradation faced in the aerospace industry. Salt-assisted material degradation was explored as it is highly applicable to war-fighting systems deployed in maritime environments, with an emphasis on Navy and Air Force systems. The tools and procedures discussed here realize the capability to execute a theoretical study on a multitude of potential next-generation structural materials that may be of interest to the Air Force and its sister services.

Appendix A. Least Squares

The parity plot for the successive adsorption energy function predicted energy values against the true energy values is given in Figure 34. The coefficient values are given in Table 7.

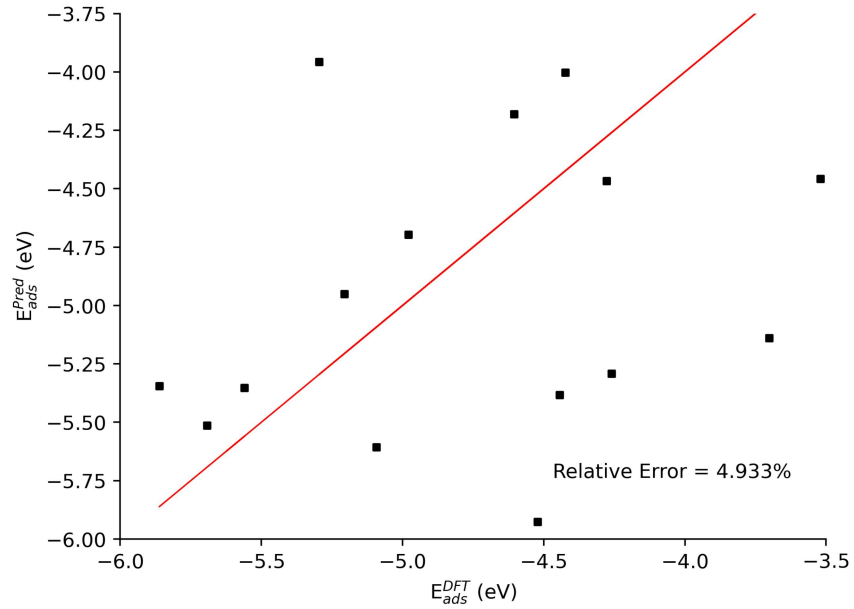


Figure 34. Parity plot for the successive adsorption energy function found using the method of least squares

Coefficients (eV)					
a	b	c	d	e	f
-1.222	-0.2170	-1.713	-1.111	-1.001	0.4322

Table 7. Coefficient values for the successive adsorption energy function found using the method of least squares

Bibliography

1. C. Niu, Y. Rao, W. Windl, and M. Ghazisaeidi, “Multi-cell Monte Carlo method for phase prediction,” *npj Computational Materials*, vol. 5, no. 1, pp. 1–5, Dec. 2019.
2. E. Antillon and M. Ghazisaeidi, “Efficient determination of solid-state phase equilibrium with the multicell Monte Carlo method,” *Physical Review E*, vol. 101, no. 6, p. 063306, Jun. 2020.
3. G. Kresse and J. Furthmüller, “Efficient iterative schemes for ab initio total-energy calculations using a plane-wave basis set,” *Physical Review B*, vol. 54, no. 16, pp. 11 169–11 186, Oct. 1996.
4. G. Kresse and D. Joubert, “From ultrasoft pseudopotentials to the projector augmented-wave method,” *Physical Review B*, vol. 59, no. 3, pp. 1758–1775, Jan. 1999.
5. H. J. Monkhorst and J. D. Pack, “Special points for Brillouin-zone integrations,” *Physical Review B*, vol. 13, no. 12, pp. 5188–5192, Jun. 1976.
6. T. Doležal, “Doležal-mc2_simcells,” https://github.com/SaminGroup/Dolezal-MC2_Simcells, released Nov 2021.
7. N. Metropolis, A. W. Rosenbluth, M. N. Rosenbluth, A. H. Teller, and E. Teller, “Equation of State Calculations by Fast Computing Machines,” *Journal of Chemical Physics*, vol. 21, pp. 1087–1092, Jun. 1953.
8. T. Doležal, “Doležal-mc2,” <https://github.com/SaminGroup/Dolezal-MC2>, released Nov 2021.
9. “SaminGroup/Dolezal-SlabGenerator,” <https://github.com/SaminGroup/Dolezal-SlabGenerator>.
10. A. Z. Panagiotopoulos, N. Quirke, M. Stapleton, and D. J. Tildesley, “Phase equilibria by simulation in the Gibbs ensemble,” *Molecular Physics*, vol. 63, no. 4, pp. 527–545, Mar. 1988.
11. A. Z. Panagiotopoulos, “Direct Determination of Fluid Phase Equilibria by Simulation in the Gibbs Ensemble: A Review,” *Molecular Simulation*, vol. 9, no. 1, pp. 1–23, Jan. 1992.

12. A. Panagiotopoulos, “Gibbs Ensemble Techniques,” in *Observation, Prediction and Simulation of Phase Transitions in Complex Fluids*, ser. NATO ASI Series, M. Baus, L. F. Rull, and J. P. Ryckaert, Eds. Dordrecht: Springer Netherlands, 1995, pp. 463–501.
13. D. G. Green, G. Jackson, E. de Miguel, and L. F. Rull, “Vapor–liquid and liquid–liquid phase equilibria of mixtures containing square-well molecules by Gibbs ensemble Monte Carlo simulation,” *The Journal of Chemical Physics*, vol. 101, no. 4, pp. 3190–3204, Aug. 1994.
14. W. Wood, “Physics of simple liquids,” *North Holland, Amsterdam*, 1968.
15. B. Smit, P. de Smedt, and D. Frenkel, “Computer simulations in the Gibbs ensemble,” *Molecular Physics*, vol. 68, pp. 931–950, Nov. 1989.
16. “VASP - Vienna Ab initio Simulation Package,” <https://www.vasp.at/>.
17. M. Born and R. Oppenheimer, “Zur Quantentheorie der Moleküle,” *Annalen der Physik*, vol. 389, no. 20, pp. 457–484, 1927.
18. P. Hohenberg and W. Kohn, “Inhomogeneous Electron Gas,” *Physical Review*, vol. 136, no. 3B, pp. B864–B871, Nov. 1964.
19. W. Kohn and L. J. Sham, “Self-Consistent Equations Including Exchange and Correlation Effects,” *Physical Review*, vol. 140, no. 4A, pp. A1133–A1138, Nov. 1965.
20. A. D. Becke, “Perspective: Fifty years of density-functional theory in chemical physics,” *The Journal of chemical physics*, vol. 140, no. 18, p. 18A301, May 2014.
21. J. Perdew, K. Burke, and M. Ernzerhof, “Generalized Gradient Approximation Made Simple,” *Physical Review Letters*, vol. 77, no. 18, pp. 3865–3868, Oct. 1996.
22. W. Quester, “Sketch pseudopotentials.png,” 22 November 2006 (original upload date), accessed on 30 Jan. 2022. [Online]. Available: https://commons.wikimedia.org/wiki/File:Sketch_Pseudopotentials.png
23. B. Cantor, I. T. H. Chang, P. Knight, and A. J. B. Vincent, “Microstructural development in equiatomic multicomponent alloys,” *Materials Science and Engineering: A*, vol. 375–377, pp. 213–218, Jul. 2004.
24. J. Yeh, S. Chen, S. Lin, J. Gan, T. Chin, T. Shun, C. Tsau, and S. Chang, “Nanostructured High-Entropy Alloys with Multiple Principal Elements: Novel Alloy Design Concepts and Outcomes,” *Advanced Engineering Materials*, vol. 6, no. 5, pp. 299–303, 2004.

25. D. B. Miracle and O. N. Senkov, “A critical review of high entropy alloys and related concepts,” *Acta Materialia*, vol. 122, pp. 448–511, Jan. 2017.
26. J. P. Couzinié, O. N. Senkov, D. B. Miracle, and G. Dirras, “Comprehensive data compilation on the mechanical properties of refractory high-entropy alloys,” *Data in Brief*, vol. 21, pp. 1622–1641, Dec. 2018.
27. O. N. Senkov, D. Isheim, D. N. Seidman, and A. L. Pilchak, “Development of a refractory high entropy superalloy,” *Entropy*, vol. 18, no. 3, Mar. 2016.
28. T. M. Butler and M. L. Weaver, “Oxidation behavior of arc melted AlCoCrFeNi multi-component high-entropy alloys,” *Journal of Alloys and Compounds*, vol. 674, pp. 229–244, Jul. 2016.
29. F. Müller, B. Gorr, H.-J. Christ, J. Müller, B. Butz, H. Chen, A. Kauffmann, and M. Heilmaier, “On the oxidation mechanism of refractory high entropy alloys,” *Corrosion Science*, vol. 159, p. 108161, Oct. 2019.
30. D. Huang, J. Lu, Y. Zhuang, C. Tian, and Y. Li, “The role of Nb on the high temperature oxidation behavior of CoCrFeMnNb_xNi high-entropy alloys,” *Corrosion Science*, vol. 158, p. 108088, Sep. 2019.
31. S. Schellert, B. Gorr, S. Laube, A. Kauffmann, M. Heilmaier, and H. Christ, “Oxidation mechanism of refractory high entropy alloys Ta-Mo-Cr-Ti-Al with varying Ta content,” *Corrosion Science*, vol. 192, p. 109861, Nov. 2021.
32. X. Shi, W. Yang, Z. Cheng, W. Shao, D. Xu, Y. Zhang, and J. Chen, “Influence of micro arc oxidation on high temperature oxidation resistance of AlTiCrVZr refractory high entropy alloy,” *International Journal of Refractory Metals and Hard Materials*, vol. 98, p. 105562, Aug. 2021.
33. X. Yang, Z. An, Y. Zhai, X. Wang, Y. Chen, S. Mao, and X. Han, “Effect of Al content on the thermal oxidation behaviour of AlHfMoNbTi high-entropy alloys analysed by in situ environmental TEM,” *Corrosion Science*, vol. 191, p. 109711, Oct. 2021.
34. C. D. Taylor, P. Lu, J. Saal, G. S. Frankel, and J. R. Scully, “Integrated computational materials engineering of corrosion resistant alloys,” *npj Materials Degradation*, vol. 2, no. 1, pp. 1–10, Feb. 2018.
35. E. Osei-Agyemang and G. Balasubramanian, “Surface oxidation mechanism of a refractory high-entropy alloy,” *npj Materials Degradation*, vol. 3, no. 1, pp. 1–8, May 2019.

36. V. Soni, O. Senkov, J. Couzinie, Y. Zheng, B. Gwalani, and R. Banerjee, “Phase stability and microstructure evolution in a ductile refractory high entropy alloy Al10Nb15Ta5Ti30Zr40,” *Materialia*, vol. 9, p. 100569, Mar. 2020.
37. A. J. Samin and C. D. Taylor, “First-principles investigation of surface properties and adsorption of oxygen on Ni-22Cr and the role of molybdenum,” *Corrosion Science*, vol. 134, pp. 103–111, Apr. 2018.
38. T. D. Doležal and A. J. Samin, “Adsorption of oxygen to high entropy alloy surfaces for up to 2 ml coverage using density functional theory and monte carlo calculations,” *Langmuir*, vol. 38, no. 10, pp. 3158–3169, 2022.
39. W. Tang, E. Sanville, and G. Henkelman, “A grid-based Bader analysis algorithm without lattice bias,” *Journal of Physics: Condensed Matter*, vol. 21, no. 8, p. 084204, Feb. 2009.
40. “Oxygen (O_2),” accessed on 01 Nov 2021. [Online]. Available: <https://janaf.nist.gov/tables/O-029.html>
41. D. Cleary, “Use of JANAF Tables in Equilibrium Calculations and Partition Function Calculations for an Undergraduate Physical Chemistry Course,” *Journal of Chemical Education*, vol. 91, pp. 848–852, May 2014.
42. A. J. Samin, “Oxidation thermodynamics of Nb-Ti alloys studied via first-principles calculations,” *Journal of Alloys and Compounds*, vol. 879, p. 160455, Oct. 2021.
43. G. Henkelman, B. P. Uberuaga, and H. Jónsson, “A climbing image nudged elastic band method for finding saddle points and minimum energy paths,” *The Journal of Chemical Physics*, vol. 113, no. 22, pp. 9901–9904, Dec. 2000.
44. R. Wu, K. Chen, D. Wang, and N. Wang, “Interaction, electron transfer, and work function of a chemisorbed alkali-metal submonolayer on a W(001) surface,” *Physical Review. B, Condensed Matter*, vol. 38, no. 5, pp. 3180–3188, Aug. 1988.
45. H. W. Hugosson, W. Cao, S. Seetharaman, and A. Delin, “Sulfur- and Oxygen-Induced Alterations of the Iron (001) Surface Magnetism and Work Function: A Theoretical Study,” *The Journal of Physical Chemistry C*, vol. 117, no. 12, pp. 6161–6171, Mar. 2013.
46. E. E. Huber and C. T. Kirk, “Work function changes due to the chemisorption of water and oxygen on aluminum,” *Surface Science*, vol. 5, no. 4, pp. 447–465, Dec. 1966.

47. Y. Guo, M. Bo, Y. Wang, Y. Liu, C. Q. Sun, and Y. Huang, “Tantalum surface oxidation: Bond relaxation, energy entrapment, and electron polarization,” *Applied Surface Science*, vol. 396, pp. 177–184, Feb. 2017.
48. M. Choi, A. Janotti, and C. G. Van de Walle, “Native point defects and dangling bonds in $\alpha\text{-Al}_2\text{O}_3$,” *Journal of Applied Physics*, vol. 113, no. 4, p. 044501, Jan. 2013.
49. F. D. Hardcastle and I. E. Wachs, “Determination of niobium-oxygen bond distances and bond orders by Raman spectroscopy,” *Solid State Ionics*, vol. 45, no. 3, pp. 201–213, Apr. 1991.
50. Y. Chen, J. L. G. Fierro, T. Tanaka, and I. E. Wachs, “Supported Tantalum Oxide Catalysts: Synthesis, Physical Characterization, and Methanol Oxidation Chemical Probe Reaction,” *The Journal of Physical Chemistry B*, vol. 107, no. 22, pp. 5243–5250, Jun. 2003.
51. D. Dodd, F. D. Hardcastle, and S. Laffoon, “Titanium-Oxygen Bond Length -Bond Valence Relationship,” vol. 67, p. 5, 2013.
52. Y. Zhang, X. Yang, and P. K. Liaw, “Alloy Design and Properties Optimization of High-Entropy Alloys,” *JOM*, vol. 64, no. 7, pp. 830–838, Jul. 2012.
53. A. J. Samin and C. D. Taylor, “A first principles investigation of the oxygen adsorption on Zr(0001) surface using cluster expansions,” *Applied Surface Science*, vol. 423, pp. 1035–1044, Nov. 2017.
54. A. Samin and C. D. Taylor, “A Combined Density Functional Theory and Monte Carlo Investigation of the Competitive Adsorption of Atomic Oxygen and Chlorine to the Ni (111) Surface,” *Journal of The Electrochemical Society*, vol. 165, no. 7, p. C302, Apr. 2018.
55. A. K. Misra and J. D. Whittenberger, “Fluoride salts and container materials for thermal energy storage applications in the temperature range 973 to 1400 K,” National Aeronautics and Space Administration, Cleveland, OH (USA). Lewis Research Center, Tech. Rep. N-87-24026; NASA-TM-89913; E-3563; NAS-1.15:89913; AIAA-87-9226; CONF-870804-39, Jan. 1987.
56. Manohar S. Sohal, Matthias A. Ebner, Piyush Sabharwall, and Phil Sharpe, “Engineering Database of Liquid Salt Thermophysical and Thermochemical Properties,” Tech. Rep. INL/EXT-10-18297, 980801, Mar. 2010.

57. K. Sridharan, T. Allen, M. Anderson, and M. Simpson, “Thermal Properties of LiCl-KCl Molten Salt for Nuclear Waste Separation,” Univ. of Wisconsin, Madison, WI (United States); Idaho National Lab. (INL), Idaho Falls, ID (United States), Tech. Rep. DOE/NEUP-09-780, Nov. 2012.
58. D. F. Williams, “Assessment of Candidate Molten Salt Coolants for the NGN-P/NHI Heat-Transfer Loop,” Oak Ridge National Lab. (ORNL), Oak Ridge, TN (United States), Tech. Rep. ORNL/TM-2006/69, Jun. 2006.
59. A. Ruh and M. Spiegel, “Thermodynamic and kinetic consideration on the corrosion of Fe, Ni and Cr beneath a molten KCl–ZnCl₂ mixture,” *Corrosion Science*, vol. 48, no. 3, pp. 679–695, Mar. 2006.
60. C. Edeleanu and R. Littlewood, “Thermodynamics of corrosion in fused chlorides,” *Electrochimica Acta*, vol. 3, no. 3, pp. 195–207, Oct. 1960.
61. J. R. Keiser, D. L. Manning, and R. E. Clausing, “Corrosion Resistance of Some Nickel-Base Alloys to Molten Fluoride Salts Containing UF₄ and Tellurium *,” *ECS Proceedings Volumes*, vol. 1976–6, no. 1, p. 315, Jan. 1976.
62. W. D. Manly, J. Adamson, J. H. Coobs, J. H. DeVan, D. A. Douglas, E. E. Hoffman, and P. Patriarca, “AIRCRAFT REACTOR EXPERIMENT–METALLURGICAL ASPECTS,” Oak Ridge National Lab., Tenn., Tech. Rep. ORNL-2349, Jan. 1958.
63. M. Kondo, T. Nagasaka, T. Muroga, A. Sagara, N. Noda, Q. Xu, D. Ninomiya, N. Masaru, A. Suzuki, and T. Terai, “High Performance Corrosion Resistance of Nickel-Based Alloys in Molten Salt Flibe,” *Fusion Science and Technology*, vol. 56, pp. 190–194, Jul. 2009.
64. M. Marecek and P. Slama, “Corrosion testing of nickel alloy for molten salt reactors,” *Journal of Achievements in Materials and Manufacturing Engineering*, vol. 70, p. 78, Jun. 2015.
65. A. Mortazavi, Y. Zhao, M. Esmaily, A. Allanore, J. Vidal, and N. Birbilis, “High-temperature corrosion of a nickel-based alloy in a molten chloride environment – The effect of thermal and chemical purifications,” *Solar Energy Materials and Solar Cells*, vol. 236, p. 111542, Mar. 2022.
66. H. Ai, X. X. Ye, L. Jiang, B. Leng, M. Shen, Z. Li, Y. Jia, J. Q. Wang, X. Zhou, Y. Xie, and L. Xie, “On the possibility of severe corrosion of a Ni-W-Cr alloy in fluoride molten salts at high temperature,” *Corrosion Science*, vol. 149, pp. 218–225, Apr. 2019.

67. S. Guo, J. Zhang, W. Wu, and W. Zhou, “Corrosion in the molten fluoride and chloride salts and materials development for nuclear applications,” *Progress in Materials Science*, vol. 97, pp. 448–487, Aug. 2018.
68. D. Ludwig, L. Olson, K. Sridharan, M. Anderson, and T. Allen, “High temperature electrochemistry of molten fluoride salt for measurement of dissolved chromium,” *Corrosion Engineering, Science and Technology*, vol. 46, no. 4, pp. 360–364, Jun. 2011.
69. J. Zhang, C. W. Forsberg, M. F. Simpson, S. Guo, S. T. Lam, R. O. Scarlat, F. Carotti, K. J. Chan, P. M. Singh, W. Doniger, K. Sridharan, and J. R. Keiser, “Redox potential control in molten salt systems for corrosion mitigation,” *Corrosion Science*, vol. 144, pp. 44–53, Nov. 2018.
70. S. Delpech, C. Cabet, C. Slim, and G. S. Picard, “Molten fluorides for nuclear applications,” *Materials Today*, vol. 13, no. 12, pp. 34–41, Dec. 2010.
71. C. A. C. Sousa and S. E. Kuri, “Relationship between niobium content and pitting corrosion resistance in ferritic stainless steels,” *Materials Letters*, vol. 25, no. 1, pp. 57–60, Oct. 1995.
72. G. Smith and N. Eisinger, “The effect of niobium on the corrosion resistance of nickel-base alloys,” *Proceedings of the International Symposium on Niobium for High Temperature Applications*, pp. 23–34, Jan. 2004.
73. R. C. Sutherlin and R. A. Graham, “Corrosion of Niobium and Niobium Alloys,” *ASM Metals Handbook - Vol. 13B Corrosion: Materials*, vol. 13B, pp. 325–336, Jan. 2005.
74. R. Prescott, F. H. Stott, and P. Elliott, “The degradation of metals in a hydrogen chloride-containing gas at high temperature,” *Corrosion Science*, vol. 29, no. 4, pp. 465–475, Jan. 1989.
75. R. M. Andrianingtyas, M. S. Anwar, S. Hastuty, I. D. Widharyanti, A. Dahliyanti, N. Prastomo, and E. Mabruri, “Role of tungsten, niobium, and vanadium on corrosion resistance of austenitic stainless steels in chloride ion environment,” *AIP Conference Proceedings*, vol. 1964, no. 1, p. 020034, May 2018.
76. Y. R. Yin, C. L. Ren, H. Han, J. X. Dai, H. Wang, P. Huai, and Z. Y. Zhu, “First-principle atomistic thermodynamic study on the early-stage corrosion of NiCr alloy under fluoride salt environment,” *Physical Chemistry Chemical Physics*, vol. 20, no. 45, pp. 28 832–28 839, 2018.

77. X. X. Ye, H. Ai, Z. Guo, H. Huang, L. Jiang, J. Wang, Z. Li, and X. Zhou, “The high-temperature corrosion of Hastelloy N alloy (UNS N10003) in molten fluoride salts analysed by STXM, XAS, XRD, SEM, EPMA, TEM/EDS,” *Corrosion Science*, vol. 106, pp. 249–259, May 2016.
78. Y. Wang, C. Zeng, and W. Li, “The influence of temperature gradient on the corrosion of materials in molten fluorides,” *Corrosion Science*, vol. 136, pp. 180–187, May 2018.
79. T. Doležal, “Dolezal-slabgenerator,” <https://github.com/SaminGroup/Dolezal-SlabGenerator>, released Nov 2021.
80. K. Momma and F. Izumi, “VESTA 3 for three-dimensional visualization of crystal, volumetric and morphology data,” *Journal of Applied Crystallography*, vol. 44, no. 6, pp. 1272–1276, Dec. 2011.
81. S. J. Zhao, L. Y. Zhou, and F. H. Wang, “First-Principles Study on Cl Adsorption on γ -TiAl(100) Surface,” *Advanced Materials Research*, vol. 803, pp. 370–374, 2013.
82. T. V. Pavlova, B. V. Andryushechkin, and G. M. Zhidomirov, “First-Principle Study of Adsorption and Desorption of Chlorine on Cu(111) Surface: Does Chlorine or Copper Chloride Desorb?” *The Journal of Physical Chemistry C*, vol. 120, no. 5, pp. 2829–2836, Feb. 2016.
83. J. Yamashita and N. Nunomura, “First-Principles Study of Chlorine Adsorption on Clean Aluminum Surface,” *Materials Science Forum*, vol. 941, pp. 1796–1801, 2018.
84. B. deB Darwent, “Bond Dissociation Energies in Simple Molecules,” NATIONAL STANDARD REFERENCE DATA SYSTEM, Tech. Rep., Jan. 1970.
85. A. Droghetti, C. D. Pemmaraju, and S. Sanvito, “Predicting d^0 magnetism: Self-interaction correction scheme,” *Physical Review B*, vol. 78, no. 14, p. 140404, Oct. 2008.
86. S. Klüpfel, P. Klüpfel, and H. Jónsson, “The effect of the Perdew-Zunger self-interaction correction to density functionals on the energetics of small molecules,” *The Journal of Chemical Physics*, vol. 137, no. 12, p. 124102, Sep. 2012.
87. “Chlorine (cl_2),” <https://janaf.nist.gov/tables/Cl-073.html>, accessed on 21 Dec 2021.

88. K. Tomihisa, Y. Kaneno, and T. Takasugi, “Phase relation and microstructure in Ni₃Al–Ni₃Ti–Ni₃Nb pseudo-ternary alloy system,” *Intermetallics*, vol. 10, no. 3, pp. 247–254, Mar. 2002.
89. K. Hagihara, T. Nakano, and Y. Umakoshi, “Deformation Twins in Ni₃Nb Single Crystals with DO₁a Structure,” *Materials Research Society Symposium - Proceedings*, vol. 646, pp. N5231–N5236, Jan. 2001.
90. A. Gabriel, H. L. Lukas, C. H. Allibert, and I. Ansara, “Experimental and Calculated Phase Diagrams of the Ni-W Co-W and Co-Ni-W System,” *International Journal of Materials Research*, vol. 76, no. 9, pp. 589–595, Sep. 1985.
91. E. B. Haugan, M. Næss, C. T. Rodriguez, R. Johnsen, and M. Iannuzzi, “Effect of Tungsten on the Pitting and Crevice Corrosion Resistance of Type 25Cr Super Duplex Stainless Steels,” *CORROSION*, vol. 73, no. 1, pp. 53–67, Jan. 2017.

REPORT DOCUMENTATION PAGE

*Form Approved
OMB No. 0704-0188*

The public reporting burden for this collection of information is estimated to average 1 hour per response, including the time for reviewing instructions, searching existing data sources, gathering and maintaining the data needed, and completing and reviewing the collection of information. Send comments regarding this burden estimate or any other aspect of this collection of information, including suggestions for reducing this burden to Department of Defense, Washington Headquarters Services, Directorate for Information Operations and Reports (0704-0188), 1215 Jefferson Davis Highway, Suite 1204, Arlington, VA 22202-4302. Respondents should be aware that notwithstanding any other provision of law, no person shall be subject to any penalty for failing to comply with a collection of information if it does not display a currently valid OMB control number. PLEASE DO NOT RETURN YOUR FORM TO THE ABOVE ADDRESS.

1. REPORT DATE (DD-MM-YYYY) 03-24-2022	2. REPORT TYPE Master Thesis	3. DATES COVERED (From — To) Sept 2020 — Mar 2022												
4. TITLE AND SUBTITLE A study on the early stages of degradation of multi-component alloy surfaces in extreme environments using the multi-cell Monte Carlo method		5a. CONTRACT NUMBER 5b. GRANT NUMBER 5c. PROGRAM ELEMENT NUMBER												
6. AUTHOR(S) Doležal, Tyler D, Capt, USAF		5d. PROJECT NUMBER 5e. TASK NUMBER 5f. WORK UNIT NUMBER												
7. PERFORMING ORGANIZATION NAME(S) AND ADDRESS(ES) Air Force Institute of Technology Graduate School of Engineering and Management (AFIT/EN) 2950 Hobson Way WPAFB OH 45433-7765		8. PERFORMING ORGANIZATION REPORT NUMBER AFIT-ENP-MS-22-M-088												
9. SPONSORING / MONITORING AGENCY NAME(S) AND ADDRESS(ES) Intentionally Left Blank		10. SPONSOR/MONITOR'S ACRONYM(S) 11. SPONSOR/MONITOR'S REPORT NUMBER(S)												
12. DISTRIBUTION / AVAILABILITY STATEMENT DISTRIBUTION STATEMENT A: APPROVED FOR PUBLIC RELEASE; DISTRIBUTION UNLIMITED.														
13. SUPPLEMENTARY NOTES														
14. ABSTRACT A computational toolset is presented and used in two examples that examined the interactions between structural materials and their extreme environments. A multi-cell Monte Carlo algorithm was developed to generate thermodynamically realistic solid-state alloy systems. These structures served as the foundation upon which surface slab models were generated. The tedious procedure of generating surface slab models from bulk structures was automated. The tools were used to study the high temperature surface corrosion resistance of a high-entropy alloy, Al10Nb15Ta5Ti30Zr40, and a nickel-based alloy, Ni70Nb10W20, under an oxygen and chlorine atmosphere, respectively. The results of this work increased the understanding of how structural systems interact with their corrosive environments at the atomic level.														
15. SUBJECT TERMS														
<table border="1" style="width: 100%; border-collapse: collapse;"> <tr> <td colspan="3" style="width: 33%; padding: 2px;">16. SECURITY CLASSIFICATION OF:</td> <td style="width: 33%; padding: 2px;">17. LIMITATION OF ABSTRACT</td> <td style="width: 34%; padding: 2px;">18. NUMBER OF PAGES</td> <td style="width: 34%; padding: 2px;">19a. NAME OF RESPONSIBLE PERSON Dr. Adib Samin, AFIT/ENP</td> </tr> <tr> <td style="width: 33%; padding: 2px;">a. REPORT U</td> <td style="width: 33%; padding: 2px;">b. ABSTRACT U</td> <td style="width: 33%; padding: 2px;">c. THIS PAGE U</td> <td style="width: 33%; padding: 2px;">UU</td> <td style="width: 34%; padding: 2px;">80</td> <td style="width: 34%; padding: 2px;">19b. TELEPHONE NUMBER (include area code) (937) 255-6565 x4581; adib.samin@afit.edu</td> </tr> </table>			16. SECURITY CLASSIFICATION OF:			17. LIMITATION OF ABSTRACT	18. NUMBER OF PAGES	19a. NAME OF RESPONSIBLE PERSON Dr. Adib Samin, AFIT/ENP	a. REPORT U	b. ABSTRACT U	c. THIS PAGE U	UU	80	19b. TELEPHONE NUMBER (include area code) (937) 255-6565 x4581; adib.samin@afit.edu
16. SECURITY CLASSIFICATION OF:			17. LIMITATION OF ABSTRACT	18. NUMBER OF PAGES	19a. NAME OF RESPONSIBLE PERSON Dr. Adib Samin, AFIT/ENP									
a. REPORT U	b. ABSTRACT U	c. THIS PAGE U	UU	80	19b. TELEPHONE NUMBER (include area code) (937) 255-6565 x4581; adib.samin@afit.edu									